Mitotic chromosomes are self-entangled and disentangle through a Topoisomerase II-dependent two stage exit from mitosis

Erica M. Hildebrand[1,6], Kirill Polovnikov[2,6], Bastiaan Dekker[1], Yu Liu[1,3], Denis L. Lafontaine[1], A. Nicole Fox[1,4], Ying Li[1], Sergey V. Venev[1], Leonid Mirny[5,7], Job Dekker[1,4,7,8]

AFFILIATIONS:

1. Department of Systems Biology, University of Massachusetts Chan Medical School, Worcester, MA, 01605

2. Independent Researcher, Moscow, Russia

3. Nuclear Dynamics and Cancer Program, Cancer Epigenetics Institute, Fox Chase Cancer Center, Temple Health, Philadelphia, PA 19111, USA

4. Howard Hughes Medical Institute, Chevy Chase, MD, 20815

5. Institute for Medical Engineering and Science, and Department of Physics, Massachusetts Institute of Technology, Cambridge, MA 02139

6. These authors contributed equally

7. Corresponding authors (Leonid@MIT.edu; Job.Dekker@umassmed.edu)

8. Lead contact (Job.Dekker@umassmed.edu)

SUMMARY

The topological state of chromosomes determines their mechanical properties, dynamics, and function. Recent work indicated that interphase chromosomes are largely free of entanglements. Here, we use Hi-C, polymer simulations and multi-contact 3C, and propose that, in contrast, mitotic chromosomes are self-entangled. We explore how a mitotic self-entangled state is converted into an unentangled interphase state during mitotic exit. Most mitotic entanglements are removed during anaphase/telophase, with remaining ones removed during early G1, in a Topoisomerase II-dependent process. Polymer models suggest a two-stage disentanglement pathway: first, decondensation of mitotic chromosomes with remaining condensin loops produces entropic forces that bias Topoisomerase II activity towards decatenation. At the second stage, the loops are released, and formation of new entanglements is prevented by lower Topoisomerase II activity, allowing the establishment of unentangled and territorial G1 chromosomes. When mitotic entanglements are not removed, in experiment and models, a normal interphase state cannot be acquired.

KEYWORDS:

Topoisomerase II, Compartment, Heterochromatin, Euchromatin, Genome Architecture, Chromosome Folding, Chromosome Entanglement, Self-Catenation, Mitosis, G1, Cohesin, Fractal Globule, Genome Topology

INTRODUCTION:

Topoisomerase II (Topo II) controls the topological state of the genome [1] throughout the cell cycle by catalyzing controlled double strand breaks and allowing DNA duplexes to pass through one another [1]. There are two forms of Topo II in the human genome, DNA Topoisomerase 2-alpha and DNA Topoisomerase 2-beta, encoded by the *TOP2A* and *TOP2B* genes, respectively [1-9]. TOP2A has well studied roles in organizing mitotic chromosomes where it is both a structural component and is required for decatenation of sister chromatids at anaphase [4,5,10-20]. TOP2B is expressed throughout the cell cycle and its activity has been detected at open chromatin sites and active chromatin including promoters and CTCF sites during interphase [1,21-25]

Whether and how the topological state of chromosomes changes during the cell cycle is not well understood. Hi-C has been widely used to characterize chromosome folding in mitosis and interphase [26]. However, since Hi-C measures pairwise interactions, one aspect of chromosome folding that is not detected by this method is the entanglement or catenation state of the genome. For the purposes of this study, we define a chromosome entanglement to be a local interlink between two regions of the genome, on the same or different chromosomes. A special type of entanglement operating on rings (loops) is a catenation; catenations can turn a ring into a knotted state or can link two rings (e.g., two chromosome loops). A catenane can also knot a linear chromosome, or a pair of chromosomes, if its ends are sufficiently far away from each other as to behave like a polymer ring. Strand passage facilitated by Topo II can both remove and create entanglements, catenating or decatenating loops. Previous

simulations of model polymers showed that highly entangled chains can become highly "intermingled". The level of intermingling can be detected using multi-contact 3C (MC-3C) [27].

MC-3C and super-resolution chromosome tracing data are consistent with interphase chromosomes being largely free of intra-chromosomal entanglements [27,28]. Hi-C data also suggest folding of interphase chromosomes into an unentangled polymer state known as the crumpled (fractal) globule [26,29,30] A recent theoretical study by some of us has revealed a universal behavior of the Hi-C contact probability curve, which is only consistent with the crumpled polymer organization with loops [31,32].

In contrast, the topological state of mitotic chromosomes is less understood. Self-entanglement is supported by in vitro experiments, isolated chromosomes, and some polymer models, with others supporting an unentangled state [33-36]. In their seminal paper A. Rosa and R. Everaers (2008) propose that the unentangled and territorial interphase state is formed by decompaction from an unentangled mitotic chromosome if Topo II is inactive during exit from mitosis [35]. Although the assumed absence of Topo II activity during interphase has been challenged by experiments, the Rosa-Everaers model highlights the importance of topological constraints in establishing and maintaining unentangled and territorial chromosomes[35].

Here we characterized the topological states of mitotic chromosomes and how cells reorganize the topological state of chromosomes upon exit from mitosis. We found that

mitotic chromosomes are highly self-entangled. We propose that cells use a two-stage process where Topo II activity eliminates these entanglements upon mitotic exit and prevent the formation of new ones, creating territorial, compartmentalized, and unentangled interphase chromosomes.

RESULTS:

Topo II inhibition leads to incomplete compartmentalization at G1 entry

Topo II has roles in formation and maintenance of mitotic chromosome structure, as well as in unlinking of sister chromatids [12,13,37]. In contrast, the relevance of Topo II for decondensation of individual chromatids after their separation and upon G1 entry is less established[38]. Here we investigated the genome-wide effect of Topo II chemical inhibition on chromosome folding and topology as cells exit mitosis and enter G1 using Hi-C, imaging, and MC-3C.

To determine whether Topo II activity is required for establishment of G1 chromosome folding, we performed Hi-C 2.0 (Hi-C) on G1 sorted cells from synchronized HeLa S3 cultures during G1 entry (Figure 1A, Figure S1H-I) [39-41]. Cells were first arrested in prometaphase using a single thymidine block + 12 hours nocodazole arrest (t = 0), and then synchronously released into G1 with either DMSO, 30uM ICRF-193, or 30uM ICRF-193 + 200uM Merbarone added at two hours post nocodazole wash-out (t = 2 hrs), when at least 50% of cells have entered or passed anaphase (Figure 1B, S1A-F). 30uM ICRF-93 is a sufficient dose to block Topo II activity as it completely prevents sister chromatid decatenation during anaphase and stabilizes Cyclin B when added

during release from a mitotic arrest (see methods,[42-44]) (Figure S1A-D). Aliquots were fixed for Hi-C using 1% formaldehyde in early G1 (*t* = 4 hrs) or late G1 (*t* = 8 hrs), and G1 cells were isolated using FACS (Figure S1A, B, E-G, I) [40,41].

In a representative prometaphase Hi-C contact map, a typical mitotic structure is observed, without visible TAD or compartment patterns (Figure 1C). In Hi-C data obtained from control (DMSO treated) cells, the checkerboard pattern representing compartmentalization is first apparent in early G1, and then becomes stronger in late G1, as previously reported (Figure 1D, H) [40,45]. In cells treated with ICRF-193 we observed two phenomena: First, at *t* = 4 hrs, we observe a very weak checkerboard and a broad diagonal of enriched interactions reminiscent of mitotic Hi-C maps (Figure 1D, Figure S2G, O) [40,44,46]. Second, at *t* = 8 hrs a nearly normal compartmentalization pattern is observed, indicating that compartments can be established but with delayed kinetics (Figure 1D). Combined addition of ICRF-193 and Merbarone, a Topo II catalytic inhibitor that acts at a different step than ICRF-193, further reduces compartment strength at *t* = 8hrs compared to ICRF-193 alone, although compartments are still somewhat increased compared to the *t* = 4 hrs timepoint (Figure 1H, Figure S1T). Merbarone alone has no effect on compartment strength (Figure S1U).

The log-ratio of Hi-C interactions detected with ICRF-193 vs. DMSO treated cells at *t* = 4 hrs shows enriched interactions close to the diagonal between A and B domains (Figure 1E), similar to what is observed in mitosis (Figure 1C) [40,44,46]. By *t* = 8 hrs, this difference is much smaller, but is retained in ICRF-193 + Merbarone treatment (Figure

1I). In addition, analysis of the relationship of interaction frequency (*P*) of pairs of loci as a function of the genomic distance (*s*) between them shows relatively frequent interactions in early G1 with ICRF-193 treatment for loci separated by 2-20Mb compared to interactions detected in untreated cells (Figure 1 F, Figure S1K, L). By late G1 (*t* = 8 hrs) *P(s)* curves are more similar, although ICRF-193 treatment still shows increased interactions in the 2-20Mb range, and this difference is more pronounced in the ICRF-193 + Merbarone condition (Figure S1V). These changes are readily detectable when the slope of *P(s)* is plotted as a function of genomic separation (*s*) (Figure 1G, Figure S1W). These data suggest that mitotic-enriched interactions are resolved only partially when cells exit mitosis in the presence of Topo II inhibitors. Finally, we quantified compartment strength at different distances. In ICRF-193 and ICRF-193 + Merbarone treated cells, A-A and B-B compartment strength is weaker in early G1 (*t* = 4 hrs) compared to DMSO treated cells, particularly for loci up to 20Mb apart (Figure 1H, I). Compartment strength partially recovers by late G1 in ICRF treated cells, but much less so when cells are treated with both inhibitors (*t* = 8 hrs). We observed no change in chromosome folding at the TAD or loop level upon Topo II inhibition by ICRF-193 (Figure S1M, N). In contrast to the mitotic exit results, Topo II inhibition does not affect steady state intra-chromosomal folding in an asynchronous (Async.) population of mainly interphase cells (Figure S1I-S). We conclude that the interphase conformation can be maintained in the presence of Topo II inhibition. In summary, Topo II activity is required during mitotic exit for complete dissolution of the mitotic state and full establishment of interphase compartments.

Disruption of compartmentalization with Topo II inhibition can be observed by confocal microscopy

We next tested whether a delay in compartmentalization upon Topo II inhibition could be observed by microscopic analysis of two histone modifications: acetylation of histone H3 lysine 27 (H3K27ac), and trimethylation of H3 lysine 9 (H3K9me3) enriched in the A or B compartments, respectively [47,48]. We fixed HeLa S3 cells to coverslips at *t* = 4 hrs and *t* = 8 hrs after mitotic release for confocal microscopy, followed by immunostaining to label H3K9me3 and H3K27ac. We also stained cells with DAPI to mark the DNA. In the DMSO treated cells, the H3K9me3 signal is highest at the periphery, as expected (Figure 2A, Figure S2A, B) [49-53]. H3K27ac is found in puncta in the interior of the nucleus, as expected for active chromatin (Figure 2A, Figure S2C) [49,51-53]. Compared to DMSO treated cells, we find that ICRF-193 treatment during G1 entry significantly increased co-localization of H3K9me3 with H3K27ac regions in early G1, corresponding to the lower compartment strength observed by Hi-C as compared to DMSO treated cells (Figure 2B). In addition, ICRF-193 treatment increases the fraction of H3K27ac signal at the nuclear periphery compared to DMSO treatment at both timepoints (Figure 2C, Figure S2C).

Topo II inhibition changes DNA morphology and Topo IIA localization in early G1

Individualized mitotic chromosomes display relatively high contrast when stained with DAPI, which we quantified by calculating the contrast of DAPI signal at a 10-pixel distance in HeLa S3 cells with Topo IIA-Venus (Figure 2D, E) [54]. As cells exit mitosis, this contrast reduces significantly as chromosomes become decondensed. In the

presence of ICRF-193 treatment we observe a significantly smaller decrease in DAPI contrast between mitotic exit (starting at *t* = 2 hrs) and early G1 (*t* = 4 hrs) as compared to control cells. Additionally, we find that endogenously tagged Topo IIA-Venus signal has the highest contrast at 2 hrs and decreases as cells enter G1 (Figure S2F). This decrease is not observed in ICRF-193 treated cells. Axial TOP2A staining was observed in some early G1 ICRF-193 treated cells (Figure 2D, see methods).

Topo II inhibition must occur early during mitotic exit to delay compartment establishment

We next tested whether the increase in compartment strength in late G1 was due to reduced ICRF-193 potency during the six-hour treatment (Figure 3A). To address this, we re-added DMSO or ICRF-193 every two hours throughout the time course and collected cells in late G1 (*t* = 8 hrs) (Figure 3B). These experiments were performed without G1 sorting, resulting in slightly larger number of cells with a G2 DNA content in populations with ICRF-193 treatment (Figure 3C, D). We observe the same phenotype in the late G1 (*t* = 8 hrs) timepoint with ICRF-193 added once or re-added every two hours (Figures 3E-J), therefore the recovery in compartment strength is not due to loss of potency of the inhibitor. Rather, ICRF-193 treatment does not inhibit all Topo II activity, and full inhibition requires use of multiple inhibitors (see above).

To determine whether there is a specific transient state in early G1 that requires Topo II activity, we added ICRF-193 at different times post mitotic release (Figure 3K-M). Comparison of the compartment strength in both the A and B compartments between

ICRF-193 and DMSO treated cells shows the largest difference for the earliest sample where ICRF-193 was added at *t* = 2 hrs, while ICRF-193 addition at *t* = 3 hrs and *t* = 4 hrs has a reduced effect on compartment establishment (Figure 3 N-Q, Figure S3J-O). Addition of ICRF-193 at *t* = 3hrs or *t* = 4hrs does not prevent further strengthening of compartments in late G1.

ICRF-193 induced delay in compartment establishment is independent of transcription

Next, we examined whether the structural defects that we observe with Topo II inhibition are related to transcription induced changes in folding, thereby interfering with reformation of G1 structure. We released HeLa S3 cells from mitosis in the presence of Triptolide (TRP) and 5,6-Dichloro-1-beta-Ribo-furanosyl Benzimidazole (DRB), which inhibit transcription initiation and elongation, respectively [55]. (Figure S3K). By Hi-C, transcription inhibition alone did not result in changes in intra-chromosomal compartment strength at any distance, and transcription inhibition did not change the ICRF-193 phenotype of decreased compartment strength in early G1 (Figure S3 M-Q, Figure S3I-N).

Mitotic chromosomes are highly intermingled, and become swiftly unmingled during mitotic exit

Previously, we showed using Multi-contact 3C (MC-3C) data that in interphase interacting compartment domains are not extensively intermingled, which is consistent with the genome being decondensed and topologically not entangled, as also inferred

from the fractal globule scaling of Hi-C data[27]. We now performed MC-3C for cells in mitosis to determine the extent of intermingling of interacting domains along mitotic chromosomes, how intermingling changes as cells exit mitosis, and how any changes depend on Topo II.

We collected synchronized cells for MC-3C at *t* = 0 (prometaphase arrest), *t* = 2 hrs after nocodazole wash-out (anaphase/telophase), and at *t* = 4 hrs/early G1 or *t* = 8 hrs/late G1 with either DMSO or 30uM ICRF-193 added at *t* = 2 hrs (Figure 4A, Figure S4A; 3 replicates). MC-3C data recapitulate the Hi-C results in terms of differences in compartmentalization and cis/trans ratio between cell cycle states and with ICRF-193 treatment (Figure 4B). Interaction distance distributions for direct pair-wise interactions derived from MC-3C data for *t* = 4 hrs and *t* = 8 hrs DMSO treated cells were similar to previously published MC-3C results in Async. cells, and Hi-C data (Figure 4C, D, Figure S4C-H) [27].

MC-3C produces “C-walks”: strings of co-occurring interactions that can provide information on the extent of intermingling between chromosomal regions. Relatively high levels of intermingling can be caused by several factors, including chromatin density, chromosome geometry, but also the presence of topological entanglements[27]. Low levels of intermingling, as we found for interphase cells[27], are consistent with the decondensed unentangled interphase state. We explored the subset of C-walks that detect interactions between two distal chromosomal domains (see Methods). C-walks at an intermingled surface will include more steps that go back and forth between the two

domains as compared to C-walks at non-intermingled surfaces (Figure 4E) [27]. The order of steps for C-walks across highly intermingled domains approaches that expected for randomized C-walks[27].

We used MC-3C data to calculate the extent of intermingling by calculating an Intermingling Metric (IM), see Methods and Figure 4 F,G. IM is the fraction of C-walks that transit between two regions of a chromosome more than once. IM can be calculated as a function of genomic distance between the interacting domains (Methods, Figure 4F). We first measured the IM in control (DMSO treated) cells during mitotic exit. Comparing the *t* = 0 prometaphase sample to late G1, we find that prometaphase chromosomes have a higher IM, with ~60% of C-walks containing more than one step connecting the two regions for most distances between two regions (Figure Gi; fully intermingled domains would be predicted, based on permutation, to have IM=0.67). In late G1, the IM is significantly lower. The effect size observed here is in line with what was observed in simulations of interactions between model polymers with entangled and unentangled interaction surfaces [27]. This result shows that chromosomes transition from a relatively intermingled to a relatively unmingled state during mitotic exit.

The IM decreases quickly as cells exit mitosis (Figure 4G). At *t* = 2 hrs (consisting of mainly anaphase/telophase cells), the IM is already greatly reduced compared to prometaphase at all distances (Figure 4Gii). At the *t* = 4 hrs early G1 timepoint the IM further decreases compared to *t* = 2 hrs anaphase/telophase, particularly at distances of

12-22 Mb between interacting domains (Figure 4Giii, iv, see bracket). This is the same distance range that has the highest level of the IM in the prometaphase sample. By *t* = 8 hrs (late G1), the IM was at the lowest level (Figure 4G)

Topo II-dependent loss of intermingling during mitotic exit suggests that mitotic chromosomes are internally catenated

We next investigated the effect of Topo II inhibition on the changes in the IM during mitotic exit. ICRF-193 treatment reduces the loss in the IM in the range of 15-20 Mb, observed from *t* = 2 hrs to *t* = 4 hrs in the DMSO treated samples (Figure 4Hi, ii). This is a similar distance range to the largest loss of compartment strength with ICRF-193 treatment by Hi-C (Figure 1J, K). However, by late G1 the IM at all distances is similar to the DMSO treated sample (Figure 4Hiii, iv), reminiscent of the compartment strength recovery by t = 8 hrs observed by Hi-C with ICRF-193 alone. The later restoration of low intermingling is probably explained by residual Topo II activity not blocked by ICRF-193, as the compartment strength does not fully recover by t = 8 hrs in the ICRF-193+Merbarone double inhibition Hi-C experiments (Fig. 1). Thus, mitotic chromosomes are internally intermingled, and during mitotic exit become decondensed and less intermingled. While high IM in mitosis can reflect, at least in part, the high level of condensation during prometaphase, the dependence of the process of unmingling during mitotic exit on Topo II suggests that decondensation involves resolution of topological entanglements.

Polymer models of G1 entry without Topo II activity support self-entangled mitotic chromatids

We turned to polymer simulations to directly test the topological state of mitotic chromosomes based on the observed effects of Topo II inhibition by Hi-C and MC-3C. We started simulations with mitotic chromosomes with or without intra-chromosomal catenations, and simulated expansion of 90 Mb chromosomes without strand passage, as in Topo II inhibited cells (see Methods). Simulated interphase organization was then compared to Hi-C results, to determine which initial catenation state is consistent with experiments.

The mitotic chromosome was modelled by a dense array of condensin loops with the average size of 400 kb, corresponding to the size of condensin II loops, that were further confined within a cylinder to reflect chromatin condensation in the mitotic environment [46]. We considered different topologies of the mitotic chromosome: an "unknotted state", with loops not catenated with each other, and a "knotted state", where loops are catenated (see Methods for details). As a global measure of catenations in a mitotic chromosome, we compute a matrix of pairwise catenations (Gaussian linking numbers) between all loop pairs (Figure 5A). While in the knotted state most loops (~70%, Figure 5A) are catenated with at least one other loop, in the unknotted state less than 3% are. Despite different topologies, the two mitotic states – knotted and unknotted – produce equivalent $P(s)$ curves (see Figure S5A).

We simulated expansion of mitotic chromosomes by releasing the cylindrical constraints and condensin loops, followed by activation of compartmental interactions and cohesin-mediated loop extrusion (see Methods). We observed very different final states when starting from knotted or unknotted mitotic states. When initiated from an unknotted state, TADs and compartments can form in G1, even without strand passage (Figure 5B, left). In contrast, when started from the knotted state where condensin loops are catenated, mitotic exit without strand passage results in a retained mitotic band of interactions close to the diagonal (Figure 5B, right) and weaker compartmental interactions, while TADs formed similarly to those in the unknotted chromosomes (Figure 5B, C). The retained mitotic band, visible on the simulated interphase contact map formed upon exit from the knotted but not from the unknotted mitotic state, closely resembles Hi-C patterns seen in Topo II inhibition experiments (Figures 5B, S5A-B and Figure 1H). This mitotic band can be also seen as a broad shoulder on the corresponding $P(s)$ curves (Figure 5D).

Presence of this mitotic band visible during interphase, seen in experiments and in simulations from the knotted mitotic state, reflects retention of mitotic entanglements in the interphase chromosomes. The same is seen in simulations without compartments, indicating that the band is not caused by compartmental interactions (Figure S5B-D). Interestingly, interphase chromosomal conformation emerging from knotted and unknotted mitotic states also have drastically different distance maps (Figure 5G-H), with loci 0.8-2 Mb apart being about 1.5-times closer in space when exiting from the knotted mitotic space. More compact chromosomes are also observed in microscopy

when cells exit mitosis in the presence of ICRF-193 (Figure 2E). In the absence of Topo II activity, initial mitotic entanglements cannot be resolved and prevent full opening of chromosomes (Videos S1-S2). This further prevents establishment of long-range interactions between homotypic compartments both at short and large distances (Figure 5C,E), consistent with experiments. Thus, simulations suggest that retention of mitotic-like morphology and weaker compartmentalization upon Topo II inhibition during mitotic exit indicate a highly self-entangled mitotic state.

Further evidence of entanglement in the mitotic state comes from comparison of territoriality of interphase chromosomes between experiments and simulations, quantified by the cis/trans ratio in simulations and MC-3C data (see Methods). Simulations that start from knotted and unknotted mitotic chromosomes, with inhibited strand passage, yield very different cis/trans ratios in the subsequent G1 phase. We calculated cis/trans ratios as a function of time, for the two initial states (Figure 5F). After several hours, the cis/trans ratios of chromosomes expanded from an unknotted mitotic state fall below the range observed experimentally upon ICRF-193 treatment (cis/trans ratio inferred from MC-3C data), see Fig. S6I. At the same time, territoriality of chromosomes expanded from a knotted mitotic state quickly saturates at values close to those observed in the Topo II inhibition experiments. This agreement between experiments and simulations additionally indicates that mitotic chromosomes are knotted.

Two-stage exit allows chromosomes to transition from an entangled mitotic to an unentangled interphase state

How can chromosomes transition from an entangled mitotic state into a largely unentangled G1 state, while establishing proper interphase organization? Our goal is to reproduce two global features of interphase chromosome organization, starting from entangled mitotic chromosomes: (i) the fractal (crumpled) globule intra-chromosomal organization measured on the *P(s)* curve; and (ii) chromosome territoriality (measured by the cis/trans ratio). The fractal globule, a compact and unknotted polymer state, is evident from the -1… -1.2 slope of the *P*(*s*) curve[26,56-60], and is best seen when cohesin-mediated loops do not obscure this scaling, e.g., upon cohesin depletion[61,62].

First, we explored a model where entangled mitotic chromosomes simply expand in the presence of high Topo II activity (modeled by having a low barrier to strand passage). In this “one-stage model”, condensin loops are released, which occurs by late telophase[40,63], with simultaneous release of cylindrical confinement of the chromosome (Figure 6A-C). Simulations show that while the knotted mitotic state rapidly expands, chromosomes extensively mix both in cis and in trans. Specifically, the fractal globule organization cannot be established as evident from the slope of the *P*(*s*) curve (Figure 6B). To better check for the fractal scaling, we remove cohesin-mediated loops in the late G1 timepoint [31,32]. We observe that the slope of the *P*(*s*) curve approaching -1.5, far below the expected -1...-1.2 for the fractal globule. This behavior is expected as high Topo II activity turns the chain into a topologically unconstrained and highly entangled nearly ideal chain (Figure 6B) [64]. Furthermore, we see that chromosomal territoriality

falls below the levels observed in MC-3C for WT interphase cells (Figure 6C and Figure S6I). Together, these results indicate that while Topo II activity allows entangled mitotic chromosomes to expand, it precludes establishment of chromosome territories and formation of the fractal globule state, as generally expected for topologically unconstrained polymers[35,64].

One-stage exit from a knotted mitotic state with Topo II activity does not reproduce the features of an unentangled interphase. In fact, while Topo II activity can allow expansion of knotted chains, its continued activity leads to mixing and does not lead to formation of the unentangled interphase. Thus, we seek a mechanism that can efficiently disentangle the mitotic state and then maintain this unentangled state later through interphase. Our key idea is that keeping mitotic loops while allowing chromosomes to decondense could entropically bias Topo II towards decatenation of the loops. This could lead to formation of the sought unentangled state, that then needs to be maintained through the rest of expansion.

On the basis of this idea, we developed a two-stage expansion process (Figure 6D). During Stage I, Topo II is active and the cylindrical constraints on the mitotic chromosome are released, while mitotic loops are still present, i.e., the nuclear environment/chromatin changes to their interphase state, but condensin loops remain. Simulations show that the first stage results in directed decatenation of condensin loops (Figure 6D-E); this is quantified using the matrices of linking numbers between the loops. A simulated chromosome is reminiscent of a swollen bottlebrush, which gradually

lengthens, as more and more loops become decatenated from each other. In 2 minutes of the first stage around 50% of mitotic catenations are removed, while at T=10 minutes after mitosis the average amount of catenations per one loop reduces almost 3-fold and reaches the topological steady-state, in which the number of newly formed catenations matches the number of removed catenations (Figure 6E). Temporal activation of Topo II activity (or delayed inhibition) for 10-20% of duration of Stage I results in rapid relaxation of catenations, with associated increase of G1 compartmental strength and decrease of territoriality (Figure S5H-J). Importantly, inducing active Topo II inside the mitotic chromosome before it starts expanding (i.e., while in the cylinder) is not able to decatenate the loops, indicating that disentanglement requires Topo II activity during expansion with intact loops (Figure S6A). Thus, directed expansion of the chains during the first stage drives repulsion between the loops, and Topo II activity mediates loop-loop decatenation.

At Stage II, the mitotic loops are released, and Topo II activity is significantly decreased. It starts with already unentangled chromosomes and maintains this state during their further expansion. Active cohesin-mediated loop extrusion and compartmentalization are also introduced at Stage II (Figure 6D). Simulations show that the remaining level of catenations from Stage I is negligible, and chromosomes form the fractal globule with a characteristic slope of $P(s)$, clearly seen upon depletion of cohesin (Figure 6I, 7F) [32,56,57,59-62,65]. The fractal globule is also evident from the visual comparison of snapshots of chromosomes colored along the chain (Figure 6D and 6A). The fractal globule is known to produce clear “intra-chromosomal territoriality” of genomic segments within a

chromosome, as seen for the two-stage exit, in contrast to mixing of segments in the case of the one-stage exit [26]. Simulations also show the fractal globule state can be formed even in the presence of some low-level of Topo II activity in Stage II (occasional strand passage) (Figure 7F). Furthermore, we find that the territoriality of simulated chromosomes after the two-stage exit agrees with that of experimental interphase MC-3C values, i.e., overlaps with the cis/trans range for chromosomes in DMSO treated cells (Figure 6F). We note that territoriality is difficult to achieve in the one stage model unless the Topo II timing is precisely fine-tuned (Figure S6G).

In the course of the second stage of our model the chromosomes become more compartmentalized, reaching the values of compartmental scores observed in DMSO experiments (Figure 6G). Similar to experiments, we also see dissolution of the mitotic band as chromosomes decompact, which is evident both in the contact maps and $P(s)$ curves (Figure 6G,H). Consistently, the mitotic band dissolves in the distance map of a chromosome (Figure 6J), in sharp contrast with the distance map obtained as a result of expansion without strand passage (Figure 5G, right).

We note that the two-stage expansion out of the hypothetical unknotted mitotic configuration would produce a qualitatively different change of compartmental strength than observed in Topo II inhibition experiments (Figure S5E-F). Indeed, the Topo II activity in Stage I would increase the number of loop-loop catenations from negligible to the level of the two-stage expansion from the knotted mitotic state (Figure S5G), yielding a less compartmentalized state than in the situation of inhibited strand passage

without catenations. This result highlights that the unknotted mitotic state is inconsistent with experimental findings on Topo II inhibition.

Taken together, the proposed two-stage mechanism of mitotic exit and decondensation facilitates large-scale chromosome disentanglement, and then maintains this unentangled state allowing the establishment of interphase organization with these hallmarks: the fractal globule, chromosome territoriality, and strong compartmentalization.

Topo II activity is required for increased compartment strength upon loss of cohesin

To test whether Topo II activity is also required for other forms of chromosome reorganization, we used the previously described HCT116 cell line carrying an auxin inducible degron (AID) and mClover fusion of RAD21, a subunit of the cohesin complex (HCT116 + RAD21-mAC cell line) [61,66-68]. In this system, depletion of cohesin results in weaker TADs and CTCF-CTCF loops, and stronger compartmentalization [61,68]. Using this system, we measured how chromosome folding is affected by the combined loss of Topo II activity and cohesin by Hi-C. We treated Async. HCT116 + RAD21-mAC cells, which are mainly in the G1 phase of the cell cycle, with 30uM of ICRF-193 to inhibit Topo II or with DMSO, and/or 500uM Auxin (Indole-3-acetic acid, IAA) to degrade RAD21 for two hours (Figure 7A, Figure S7A). Following fixation, the cell populations were sorted for G1 DNA content, and +/- mClover expression (Figure S7B,C).

As previously observed, short-range Hi-C interactions are decreased, while long-range compartment-specific interactions are increased with RAD21 degradation (Figure 7B, C) [61]. The loss of cohesin-mediated loop extrusion can be observed by a loss of the peak in the derivative of *P(s)* at ~100 kb, and loss of TADs on 50kb binned heatmaps (Figure 7B, C, Figure S7D-F,H) [32,69,70]. RAD21 depletion + ICRF-193 did not significantly changes the *P(s)* curves compared to RAD21 depletion alone. RAD21 depletion alone reduces loop strength, as previously published [61], while ICRF-193 treatment alone has no effect on looping interactions, nor on the effect of cohesin depletion [IAA + ICRF-193] (Figure 7D).

Simulations of cohesin depletion in late interphase, obtained through the two-stage process with some weak Topo II activity in Stage II (see Methods), recapitulate the subtle effects of Topo II inhibition observed in $P(s)$ curves (Figure 7F); importantly, the model suggests that some Topo II activity in Stage II can still reproduce the fractal scaling of $P(s)$ observed experimentally (Figure 7G,H), as long as this activity is sufficiently weak.

Compartment strength is increased with RAD21 degradation (Figure 7I-L, FigureS7G) [61,69,70]. However, the compartment strength increase observed with IAA treatment is partially blocked by the addition of ICRF-193, particularly in the B compartment (Figure 7L). Treatment with ICRF-193 alone has only minimal effects on compartment strength, as also observed in the Async HeLa S3 cell line (see Figure S1K,L). We observe similar results in the simulations: while complete inhibition of strand passage alone marginally

affects compartmentalization of the interphase chains, in combination with cohesin depletion it yields lower compartmental scores than in the situation of cohesin depletion only (Figure 7M,N). Therefore, weak Topo II activity contributes to the transition in chromosome folding at the compartment scale upon the loss of cohesin.

Importantly, these results reveal two features of the interphase genome: first, loss of cohesin-mediated loops reveal a crumpled chromatin state consistent with an unentangled conformation. Second, the fact that the increase in compartmentalization upon loss of cohesin is partly dependent on Topo II activity suggests Topo II activity during interphase. The two features are consistent with each other as long as the interphase Topo II activity is sufficiently weak, see Figure 7H.

DISCUSSION

The mitotic chromosome is internally entangled

Whether intra-chromosomal entanglements occur in mitotic chromosomes has long been an open question in the field, due to an inability to directly measure entanglements in endogenous chromosomes. An unentangled mitotic state has long been the dominant view, as it would naturally expand into an unentangled interphase, which is observed experimentally, assuming strand passage is not active [34,35]. However, our results demonstrate that artificial inhibition of Topo II during mitotic exit results in dramatic changes in the subsequent interphase structure. Our polymer simulations show that these experimentally observed changes can be reconciled with an entangled mitotic chromosome that requires Topo II activity to expand into interphase.

Entangled mitotic chromosomes have been previously predicted to form a stiffer structure than unentangled chromosomes, which may be important for ensuring proper chromosome segregation[33]. A recent study using in vitro mitotic chromosome reconstitution in Xenopus egg extracts showed that Topo II activity is required to increase chromosome thickness when condensin is present but results in inter-chromosome entanglements when condensin is depleted[71]. This model of mitotic intra-chromosomal entanglements mediated by Topo II directed by condensin to form mitotic chromosomes is consistent with our entanglement measurements during mitosis[71].

Two-stage exit from mitosis

Formation of an unentangled interphase organization from an entangled mitotic chromosome poses a serious challenge: While Topo II activity is required for expansion and compartmentalization, at the same time it prevents the establishment of hallmarks of interphase organization such as chromosome territories and the unentangled fractal globule state. Polymer simulations show that this paradox can be resolved by a two-stage mitotic exit where chromosomes first become unentangled and then are maintained at this state.

In the first stage, decompaction of mitotic chromosomes with mitotic (condensin) loops still present produces a swollen bottlebrush conformation. Loops in this state entropically repel each other, biasing Topo II towards decatenation. As we find in time-calibrated simulations, Topo II needs to be active for ~10-20 min to largely

disentangle condensin loops; this time is close to the condensin residence time [72,73]. In the second stage, the disentangled chromosomes expand upon the loss of condensin loops, yet with reduced Topo II activity, allowing to maintain the unentangled state, and thus enabling formation of territorial and fractal globule chromosomes. In accord with our cohesin depletion experiments in G1, polymer simulations further demonstrate that some weak Topo II activity in the second stage is consistent with a largely unentangled interphase organization (Figure 7G).

In a recent synchronized Hi-C study on mitotic exit, the existence of a loop-free, and possibly unentangled state was demonstrated during telophase, when most of the condensins have dissociated and cohesin has not re-associated with chromatin [40]. This importantly suggests that the disentanglement of mitotic chromosomes takes place during the stage after the metaphase-to-anaphase transition and before the condensins are released from chromosomes. Our current experiments further highlight an important role of Topo II in these early stages of mitotic exit, as its early inhibition results in retention of mitotic-like organization in the following interphase (Figures 1-3). Consistent with these experimental observations, the two-stage model of mitotic exit demonstrates that most of the mitotic entanglements can be removed via decompaction of mitotic chromosomes with condensin loops under high Topo II activity (Stage I). Thus, a swollen bottlebrush state is likely present until telophase onset and linked to decatenation of mitotic loops.

Taken together, our work shows that cells control the entanglement state of the genome during mitotic exit, with important roles for chromosome loops, chromatin decondensation, and regulation of Topo II activity levels.

Our study makes several predictions that future experiments can test. First, the two-stage mechanism suggests the presence of a transient state with associated condensins, expanded mitotic-like state, and high Topo II activity. Detection and characterization of this state, with its unique morphology, chromatin associated condensins and Topo II is a challenge for live-cell microscopy. Second, our models suggest that Topo II inhibition can keep chromosomes in a similar partially expanded mitotic-like state even after condensin loops are gone. We predict how distance maps accessible by high-resolution microscopy[74] would appear, and how the scaling of the spatial distance with genomic separation would be affected by Topo II inhibition.

Limitations of the study

First, our study uses chemical inhibition of Topo II activity. ICRF-193 leads to immobilization of Topo II on chromatin, and this may affect chromosome conformation in unknown ways. Alternative methods include the use of degron-based removal of Topo II, but such methods lack the temporal control required for study of chromosome folding dynamics during mitotic exit, when topoisomerases are also required to separate sister chromatids. Second, our proposal that mitotic chromosomes are self-entangled is based on the combined integration of polymer modelling and the analysis of experimental effects of Topo II inhibition (Hi-C, MC-3C data, imaging data). We do not

have direct experimental data showing that mitotic loops are catenated. For instance, while MC-3C data show high levels of intermingling of chromatin within condensed prometaphase chromosomes, and a dependence on Topo II activity for unmingling during decondensation, the chromatin interaction data by itself is not providing direct evidence for topological entanglements. Experimental evidence for catenation of mitotic loops will await development of imaging-based methods with sufficient resolution and scale to trace individual loops at nm resolution in 3D. Third, although the proposed two-stage mechanism of mitotic exit seems to be a natural way to disentangle the chromosomes via involvement of regulated topoisomerase activity, it is only tested by polymer modeling.

ACKNOWLEDGEMENTS

We are grateful to Masato Kanemaki for kindly providing the HCT-116-Rad21-mAID-mClover cell line. We thank several UMass Chan Medical School Facilities for their assistance, including Christina Baer at the Sanderson Center for Optical Experimentation, the Deep Sequencing Core, the PacBio Core Enterprise, the Molecular Biology Core Labs, and the Flow Cytometry Core. We thank Caryn Navarro, Caroline Austin, and members of J.D.'s and L.M.'s groups for helpful discussions and comments on the manuscript. Diagrams included in figures were created with BioRender.com. Experiments in this study used a HeLa cell line. Henrietta Lacks, and the HeLa cell line that was established from her tumor cells without her knowledge or consent in 1951, have made significant contributions to scientific progress and

advances in human health. We are grateful to Henrietta Lacks, now deceased, and to her surviving family members for their contributions to biomedical research. We also thank the anonymous patient who contributed the HCT 116 cell line used in this study. We acknowledge support from the National Science Foundation (NSF-ANR Physics of chromosomes through mechanical perturbations; NSF 2210558 ANR-22-CE95-0003), the National Institutes of Health Common Fund 4D Nucleome Program (DK107980, HG011536), the National Human Genome Research Institute (HG003143) and the National Institute of General Medical Sciences (R01GM114190). J.D. is an investigator of the Howard Hughes Medical Institute. E.H. was supported by an F32 fellowship from the NIH (F32-CA224689). The work of K.P. is supported by the Russian Science Foundation (Grant No. 21-73-00176). K.P. acknowledges support of the Programme d'investissements d'avenir (LabEx DEEP) at Institut Curie, Paris, France, and the hospitality of LPTMS laboratory (University of Paris-Saclay), where part of this work was done.

PUBLISHED DATASETS USED

4DNFIFLDVASC, 4DNFIBM9QCFG

AUTHOR CONTRIBUTIONS

Conceptualization, EH, JD, KP, and LM. Methodology, EH, KP, NF, YLiu. Software, EH, KP, BD, SV. Validation, EH, YLiu. Formal Analysis, EH, KP. Investigation, EH, YLiu, BD, NF, DL, YLing. Data Curation, EH. Writing – Original Draft, EH. Writing – Review and Editing, EH, JD, KP, LM. Visualization, EH, KP. Supervision, JD, LM. Funding acquisition, JD, LM, EH, KP.

COMPETING INTERESTS

J.D. is on the scientific advisory board of Arima Genomics and Omega Therapeutics.

FIGURE LEGENDS:

Figure 1: Topo II inhibition by ICRF-193 delays compartment re-establishment at G1 entry

A. Schematic of HeLa S3 mitotic synchronization and release experiment with Topo II inhibition.

B. Cell cycle profiles by PI staining and flow cytometry of cells for Hi-C experiment shown in in D-G (N = 2).

C. Hi-C interaction heatmap and Eigenvector 1 of unsorted HeLa S3 cells from nocodazole arrest (*t* = 0, prometaphase), from a separate experiment as an example.

D. Hi-C interaction heatmaps and Eigenvector 1 of G1 sorted MR HeLa S3 cells treated with DMSO or 30uM ICRF-193, two replicates combined.

E. Hi-C interaction log10 ratio heatmap comparing ICRF-193 treatment to DMSO control for each timepoint.

F. *P(s)* scaling plot of G1 sorted HeLa S3 cells (Async, MR, and Prometaphase samples from separate experiments).

G. First derivative (slope) of *P(s)* scaling plot shown in F.

H. Hi-C interaction heatmaps and Eigenvector 1 of G1 sorted MR HeLa S3 cells treated with DMSO or 30uM ICRF-193 + 200uM Merbarone, N = 1.

I. Hi-C interaction log10 ratio heatmap comparing ICRF-193 + Merbarone treatment to DMSO control for each timepoint, N = 1.

J. AA compartment strength log2 ratio compared to control at each collection time by distance, for G1 sorted HeLa S3 cells treated with ICRF-193. N = 2. (AS and MR from separate experiments, as above).

K. BB compartment strength log2 ratio compared to control at each collection time by distance, for G1 sorted HeLa S3 cells treated with ICRF-193, as in J.

L. AA compartment strength log2 ratio compared to control at each collection time by distance, for G1 sorted HeLa S3 cells treated with ICRF-193 + Merbarone. N = 1.

M. BB compartment strength log2 ratio compared to control at each collection time by distance, for G1 sorted HeLa S3 cells treated with ICRF-193 + Merbarone. N = 1.

Figure 2: ICRF-193 treatment during G1 entry disrupts nuclear organization and chromosome morphology

A. Representative confocal microscopy images in Early (*t* = 4 hrs) and Late (*t* = 8 hrs) G1 HeLa S3 cells after mitotic release with either DMSO or 30uM ICRF-193 treatment from *t* = 2 hrs post nocodazole washout. i. merge of all channels. Ii. merged image with an overlay (white lines) of the H3K27ac segmented objects containing H3K9me3 objects, as used for quantification of overlap between the two types of chromatin in B. iii. DAPI, iv. H3K27ac, v. H3K9me3.

B. Boxplot of the fraction of H3K27ac segmented regions that contain H3K9me3 segmented for each nucleus.

C. Boxplot of the mean fraction of H3K27ac signal in the outermost (peripheral) radial bin, out of 10 total bins.

D. Representative confocal microscopy images in a mitotic release timecourse with DMSO or ICRF-193 treatment (30uM) starting at *t* = 2 hrs post mitotic release. i. Merged images. ii. DAPI, iii. TOP2A-Venus, iv. Lamin A.

E. Boxplot of DAPI signal contrast in each nucleus, at a distance of 10 pixels.

Figure 3: Topo II inhibition must occur during mitotic exit to delay compartment establishment

A. Schematic of HeLa S3 mitotic synchronization and release Hi-C experiment with ICRF-193 treatment starting at *t* = 2 hrs, collected at *t* = 4 hrs (early G1) or *t* = 8 hrs (late G1), without sorting.

B. Schematic of HeLa S3 mitotic synchronization and release Hi-C experiment with ICRF-193 treatment starting at *t* = 2 hrs, re-added at *t* = 4 hrs and *t* = 6 hrs, collected at *t* = 8 hrs (late G1), without sorting.

C. Cell cycle profiles by PI staining and flow cytometry of cells described in A before G1 sorting. (N = 2).

D. Cell cycle profiles by PI staining and flow cytometry of cells described in B before G1 sorting. (N = 2).

E. Hi-C interaction heatmaps and Eigenvector 1 of unsorted HeLa S3 cells treated with DMSO, ICRF-193 at *t* = 2 hrs and collected at *t* = 4 hrs or *t* = 8 hrs. Two replicates combined.

F. Hi-C interaction heatmaps and Eigenvector 1 of unsorted HeLa S3 cells treated with DMSO or ICRF-193 added at *t* = 2 hrs, and readded at *t* = 4 hrs, and *t* = 6 hrs, and collected at *t* = 8 hrs. Two replicates combined.

G. Hi-C interaction log10 ratio heatmap comparing ICRF-193 treatment to DMSO control for each treatment type in E.

H. Hi-C interaction log10 ratio heatmap comparing ICRF-193 treatment to DMSO control for samples in F.

I. AA Hi-C compartment strength log2 ratio compared to DMSO by distance, separated by compartment type, for HeLa S3 cells described in A and B. N=2. With and without re-adding samples are from separate experiments.

J. BB Hi-C compartment strength log2 ratio compared to DMSO by distance, separated by compartment type, for HeLa S3 cells described in A and B. N=2. With and without re-adding samples are from separate experiments.

K. Schematic of HeLa S3 mitotic synchronization and release experiment with ICRF-193 treatment starting at *t* = 2 hrs, *t* = 3 hrs, or *t* = 4 hrs post mitotic release, collected after 5 hours of treatment, with sorting for G1 DNA content.

L. Flow cytometry profiles for DNA content (PI stain) of synchronized HeLa S3 cells as in I released into G1 at *t* = 2 hrs, *t* = 3 hrs, or *t* = 4 hrs, at the time of ICRF-193 addition. One representative replicate shown.

M. Cell cycle profiles by PI staining and flow cytometry of cells described in K before G1 sorting. (N = 2).

N. Hi-C interaction heatmaps and Eigenvector 1 of G1 sorted MR HeLa S3 cells treated with DMSO or 30uM ICRF-193 from *t* = 2 hrs to *t* = 7 hrs, *t* = 3 hrs to *t* = 8 hrs, or *t* = 4 hrs to *t* = 9 hrs after mitotic release. Two replicates combined.

O. Hi-C interaction log10 ratio heatmap comparing ICRF-193 treatment to DMSO control for each treatment type. Two replicates combined.

P. AA Hi-C compartment strength log2 ratio compared to DMSO by distance, separated by compartment type, for HeLa S3 cells described in K. N=2.

Q. BB Hi-C compartment strength log2 ratio compared to DMSO by distance, separated by compartment type, for HeLa S3 cells described in K. N = 2.

Figure 4: Topo II resolves mitotic entanglements during G1 establishment of interphase chromosome folding

A. Schematic of cell synchronization and MC-3C protocol. MC-3C was performed on HeLa S3 cells during prometaphase arrest (*t* = 0) or after mitotic release at *t* = 2 hrs (anaphase/telophase), *t* = 4 hrs (early G1), or *t* = 8 hrs (late G1). The early and late G1 timepoints had DMSO or 30uM ICRF-193 added at *t* = 2 hrs post mitotic release, and were G1 sorted after fixation.

B. Fraction of C-walks within one chromosome or between two chromosomes, and in A, B, or both A and B compartments. Three biological replicates.

C. Density plot of the direct pairwise interaction distances from MC-3C C-walks, N = 3. Bracket shows the region where ICRF-193 treatment results in retained mitotic interactions in early G1 compared to DMSO treatment (Figure 1).

D. Density plot of pairwise interaction distance from sampled Hi-C libraries made from *t* = 0 prometaphase and *t* = 2 hrs anaphase/telophase unsorted cells, and G1 sorted early and late G1 cells with DMSO or 30uM ICRF-193 treatment. t = 0 and t = 2 hrs samples are from a separate experiment from t = 4 hrs and t = 8 hrs samples. Bracket shows the region where ICRF-193 treatment results in retained mitotic interactions compared in early G1 compared to DMSO treatment.

E. Schematic of types of interfaces between different genomic regions on the same chromosome. A smooth interface (top) will result in a C-walk (black dashed arrow) with most steps within each region, and fewer steps between the two regions (indicated by small black solid arrow). An entangled/intermingled interface (bottom) will result in a C-walk (black dashed arrow) with more steps between the two regions (indicated by small black solid arrows).

F. i. Formula of the IM calculation for determining how much intermingling/entanglement occurs between two regions. The IM is calculated as the fraction of C-walks with >1 inter-region step.

F. ii. Schematic of the two possible types of two region C-walks considered for calculation of the Intermingling Metric (IM). Regions are defined as either side of the largest step (x) within each C-walk, with each side extending ¼ of the size of the largest step upstream and downstream of the midpoint of fragment at either end of the largest step (so each region has a maximum size of ½ the largest step size ($0.5x$)).

G. Intermingling analysis of control cells during mitotic exit. Pairwise comparisons of the IM at 12Mb window size. Mean (darker line) +/- 95% CI (lighter filled areas) of three biological replicates is shown for the real C-walks. Permuted C-walks (100 permutations per sample x 3 replicates each) are also plotted, with the mean of all 300 permutations for each sample shown as dashed lines, and 95% CI shown by the surrounding filled areas. Arrows in i. indicate low intermingling (blue), medium-high intermingling (purple), and highest intermingling (red). Bracket in iv. indicates the area of significant difference between t = 2 hrs and t = 4 hrs early G1 DMSO.

H. Intermingling analysis of ICRF-193 treated cells, pairwise comparisons to DMSO or t = 2hrs samples plotted as in G. Bracket indicates the area of significant difference between *t* = 4 hrs early G1 DMSO and *t* = 4 hrs early G1 ICRF-193.

Figure 5. Polymer simulations reveal that hallmarks of mitotic exit with inhibited Topo II correspond to the entangled mitotic chromosome

A. Two topologies of mitotic state considered in polymer simulations. Contact maps and matrices of the Gaussian linking numbers for the loop pairs are shown for each state. The snapshots of the two states are demonstrated: condensin loops (gray) form a dense bottlebrush array; condensins in the loop bases comprise the spiraled backbone (red); two individual loops (non-catenated in the left and catenated in the right) are shown by magenta and green.

B. The simulated contact matrices for unknotted (left) and knotted (right) initial states for early (1-2 hour) and late (6-8 hours) interphase.

C. The compartmental saddle plots and the corresponding compartmental scores for the contact matrices from panel B at scales 0.75-20Mb are demonstrated. See STAR Methods for more details.

D. The contact probability curves and the log-derivatives for the two initial states at different timepoints in G1 as indicated in the legend on the panel E. The gray dashed curve corresponds to mitosis.

E. Interphase compartmental scores for the exits from the two mitotic states (top) and the corresponding log2-ratios (bottom) computed for two timepoints in G1, see the

legend. Each dot represents a value for the interphase contact map averaged over 16 mitotic replicates and the bars represent the mean value.

F. Kinetics of the chromosomal territoriality for the two initial states (knotted – red, unknotted – cyan), measured as cis/trans ratio in simulations.

G. Distance maps for the early G1 timepoint out of the two mitotic states.

H. The plots of the mean squared end-to-end distances $R^2(s)$ for the interphase segments of length s obtained from the two mitotic states.

Figure 6. The two-stage model of mitotic exit allows for directed Topo II and removal of most of the mitotic catenations

(A-C): one-stage exit. (D-J): two-stage exit.

A. Schematic for the one-stage exit.. Such an exit results in internal mixing of the chains, as shown by the disordered organization of the colored interphase chain on the right.

B. The log-derivative of the average contact probability $P(s)$ computed after removal of cohesin loops at the late G1 timepoint (bold gray curve; different replicates are shown by thin gray lines). The experimental range of the $P(s)$ slopes between -1.15 and -1, corresponding to the fractal globule (FG) state, is shown by pink.

C. Snapshots of three overlapping chromosomes (PBC images) from one-stage simulations (left). The cis/trans ratio as the function of the exit time (right).

D. Schematic for the two-stage exit. The matrices of the linking number for the condensin loop pairs are shown in the knotted mitotic state and by the end of Stage I;

magenta and blue dashed lines correspond to the two loops that are catenated in the mitosis, but decatenate during Stage I.

E. Mean number of catenations per loop as a function of duration of the first stage (bold black curve; 16 replicates are shown by thin gray lines). The red dashed line denotes the steady-state number of residual catenations ~0.25. This steady-state is achieved in $T \approx 10$ minutes, which is used in further analysis of the two-stage exit.

F. Snapshots of three weakly overlapping chromosomes (PBC images) from two-stage simulations (left). The cis/trans ratio as the function of the exit time (right).

G. Interphase contact maps for early and late timepoints, obtained via the two-stage exit (top). The corresponding compartmental saddle plots with the compartmental scores are shown in the bottom.

H. The interphase $P(s)$ and its log-derivative for the two-stage exit at two timepoints (cyan) and for the exit with inhibited strand passage from the knotted initial state (red). The dashed black curves correspond to the mitotic state.

I. The log-derivative of $P(s)$ computed after removal of cohesin loops at the late G1 timepoint. The curves corresponding to the two-stage exit is shown by cyan, while the curves for the exit with inhibited strand passage from knotted and unknotted states are shown by red and dark cyan, correspondingly. The experimental range of the $P(s)$ slopes between -1.15 and -1, corresponding to the fractal globule (FG) state, is shown by pink.

J. Distance map for the early G1 timepoint obtained via the two-stage process.

Figure 7: Weak Topo II is required for increased compartment strength due to cohesin degradation

A. Schematic of RAD21 degradation and Topo II inhibition by ICRF-193 in AS HCT116 + RAD21-AID-mClover (HCT116 + RAD21-mAC) cells for Hi-C. Cells were treated for 2 hours with IAA and/or ICRF-193 before fixation for Hi-C, and sorting for G1 DNA content with (- IAA samples) or without (+ IAA samples) mClover.

B. P(s) scaling plot of G1 sorted HCT116 + RAD21-mAC cells described in A. N = 3.

C. First derivative (slope) of P(s) scaling plot shown in B. N = 3.

D. Aggregate loop pileup (APA) of experiment shown in A at dots called in published high resolution Hi-C data from HCT116 + RAD21-mAC (Untreated) (4DNFIFLDVASC). Average log2(observed/expected). N = 3.

E. Log2 fold change of APA for each treatment vs the control

F. The $P(s)$ log-derivatives computed for simulations of four states: unperturbed interphase obtained via the two-stage process with low activity of Topo II ($e_{tr} = 5kT$), interphase with further inhibited Topo II (ΔTopo II; $e_{tr} = 10kT$), interphase with further depleted cohesin loops but remained low activity of Topo II (ΔCohesin; $e_{tr} = 5kT$), interphase with depleted cohesin loops and inhibited Topo II (ΔTopo II, ΔCohesin; $e_{tr} = 10kT$).

G. Simulations of various levels of the strand passage activity during Stage II of the two-stage exit, as modelled by varying the excluded volume barrier. The graph shows the log-derivatives of the contact probability P(s) in interphase after depletion of cohesin loops (late G1). The red strip shows the range of experimental log-derivatives between –1.15 and –1 (panel C).

H. A model: Depletion of cohesin loops in the interphase state allows to assess the topological state of chromosomes from the log-derivative of P(s). The slopes around -1 correspond to the fractal organization, which is only consistent with sufficiently weak activity of Topo II in the interphase.

I. Experimental Hi-C interaction heatmaps and Eigenvector 1 of HCT116 + RAD21-mAC cells described in A, three replicates combined.

J. Hi-C interaction log2 ratio comparing each treatment to the Control or to the IAA treatment, as indicated. Three replicates combined.

K. AA compartment strength log2 ratio compared to Control by distance for HCT116 + RAD21-mAC cells, N=3.

L. BB compartment strength log2 ratio compared to Control by distance for HCT116 + RAD21-mAC cells, N=3.

M. Contact maps and the corresponding compartmental saddle plots from simulations for four states described in F.

N. The log2 ratios of the compartment score in perturbed and unperturbed interphase simulations at short and large genomic scales. Each dot represents a ratio computed for a pair of perturbed and unperturbed contact maps, both averaged over 16 replicates. The bars represent the corresponding mean values.

STAR METHODS:

Resource availability

Lead contact

REFERENCES

1. Pommier, Y., Sun, Y., Huang, S.N., and Nitiss, J.L. (2016). Roles of eukaryotic topoisomerases in transcription, replication and genomic stability. Nat Rev Mol Cell Biol *17*, 703-721. 10.1038/nrm.2016.111.
2. Austin, C.A., and Fisher, L.M. (1990). Isolation and characterization of a human cDNA clone encoding a novel DNA topoisomerase II homologue from HeLa cells. FEBS Lett *266*, 115-117. 10.1016/0014-5793(90)81520-x.
3. Lewis, C.D., and Laemmli, U.K. (1982). Higher order metaphase chromosome structure: evidence for metalloprotein interactions. Cell *29*, 171-181. 10.1016/0092-8674(82)90101-5.
4. Earnshaw, W.C., and Heck, M.M. (1985). Localization of topoisomerase II in mitotic chromosomes. J Cell Biol *100*, 1716-1725. 10.1083/jcb.100.5.1716.
5. Earnshaw, W.C., Halligan, B., Cooke, C.A., Heck, M.M., and Liu, L.F. (1985). Topoisomerase II is a structural component of mitotic chromosome scaffolds. J Cell Biol *100*, 1706-1715. 10.1083/jcb.100.5.1706.
6. Drake, F.H., Zimmerman, J.P., McCabe, F.L., Bartus, H.F., Per, S.R., Sullivan, D.M., Ross, W.E., Mattern, M.R., Johnson, R.K., Crooke, S.T., and et al. (1987). Purification of topoisomerase II from amsacrine-resistant P388 leukemia cells. Evidence for two forms of the enzyme. J Biol Chem *262*, 16739-16747.
7. Wang, J.C. (2002). Cellular roles of DNA topoisomerases: a molecular perspective. Nat Rev Mol Cell Biol *3*, 430-440. 10.1038/nrm831.
8. Austin, C.A., Barot, H., Margerrison, E.E.C., Hayes, M.V., and Fisher, L.M. (1989). Biochemical and immunological characterization of mammalian DNA topoisomerase II. Biochemical Society Transactions *17*, 528-529. 10.1042/bst0170528.
9. Tsai-Pflugfelder, M., Liu, L.F., Liu, A.A., Tewey, K.M., Whang-Peng, J., Knutsen, T., Huebner, K., Croce, C.M., and Wang, J.C. (1988). Cloning and sequencing of cDNA encoding human DNA topoisomerase II and localization of the gene to chromosome region 17q21-22. Proc Natl Acad Sci U S A *85*, 7177-7181. 10.1073/pnas.85.19.7177.
10. Broderick, R., and Niedzwiedz, W. (2015). Sister chromatid decatenation: bridging the gaps in our knowledge. Cell Cycle *14*, 3040-3044. 10.1080/15384101.2015.1078039.
11. Bower, J.J., Karaca, G.F., Zhou, Y., Simpson, D.A., Cordeiro-Stone, M., and Kaufmann, W.K. (2010). Topoisomerase IIalpha maintains genomic stability through decatenation G(2) checkpoint signaling. Oncogene *29*, 4787-4799. 10.1038/onc.2010.232.
12. Luo, K., Yuan, J., Chen, J., and Lou, Z. (2009). Topoisomerase IIalpha controls the decatenation checkpoint. Nat Cell Biol *11*, 204-210. 10.1038/ncb1828.
13. Samejima, K., Samejima, I., Vagnarelli, P., Ogawa, H., Vargiu, G., Kelly, D.A., de Lima Alves, F., Kerr, A., Green, L.C., Hudson, D.F., et al. (2012). Mitotic chromosomes are compacted laterally by KIF4 and condensin and axially by topoisomerase IIalpha. J Cell Biol *199*, 755-770. 10.1083/jcb.201202155.

14. Warburton, P.E., and Earnshaw, W.C. (1997). Untangling the role of DNA topoisomerase II in mitotic chromosome structure and function. Bioessays *19*, 97-99. 10.1002/bies.950190203.
15. Moens, P.B., and Earnshaw, W.C. (1989). Anti-topoisomerase II recognizes meiotic chromosome cores. Chromosoma *98*, 317-322. 10.1007/BF00292383.
16. Heck, M.M., and Earnshaw, W.C. (1986). Topoisomerase II: A specific marker for cell proliferation. J Cell Biol *103*, 2569-2581. 10.1083/jcb.103.6.2569.
17. Heck, M.M., Hittelman, W.N., and Earnshaw, W.C. (1988). Differential expression of DNA topoisomerases I and II during the eukaryotic cell cycle. Proc Natl Acad Sci U S A *85*, 1086-1090. 10.1073/pnas.85.4.1086.
18. Gasser, S.M., Laroche, T., Falquet, J., Boy de la Tour, E., and Laemmli, U.K. (1986). Metaphase chromosome structure. Involvement of topoisomerase II. J Mol Biol *188*, 613-629. 10.1016/s0022-2836(86)80010-9.
19. Gasser, S.M., and Laemmli, U.K. (1986). The organisation of chromatin loops: characterization of a scaffold attachment site. EMBO J *5*, 511-518. 10.1002/j.1460-2075.1986.tb04240.x.
20. Mirkovitch, J., Gasser, S.M., and Laemmli, U.K. (1988). Scaffold attachment of DNA loops in metaphase chromosomes. J Mol Biol *200*, 101-109. 10.1016/0022-2836(88)90336-1.
21. Canela, A., Maman, Y., Huang, S.N., Wutz, G., Tang, W., Zagnoli-Vieira, G., Callen, E., Wong, N., Day, A., Peters, J.M., et al. (2019). Topoisomerase II-Induced Chromosome Breakage and Translocation Is Determined by Chromosome Architecture and Transcriptional Activity. Mol Cell *75*, 252-266 e258. 10.1016/j.molcel.2019.04.030.
22. Canela, A., Maman, Y., Jung, S., Wong, N., Callen, E., Day, A., Kieffer-Kwon, K.R., Pekowska, A., Zhang, H., Rao, S.S.P., et al. (2017). Genome Organization Drives Chromosome Fragility. Cell *170*, 507-521 e518. 10.1016/j.cell.2017.06.034.
23. Canela, A., Sridharan, S., Sciascia, N., Tubbs, A., Meltzer, P., Sleckman, B.P., and Nussenzweig, A. (2016). DNA Breaks and End Resection Measured Genome-wide by End Sequencing. Mol Cell *63*, 898-911. 10.1016/j.molcel.2016.06.034.
24. Uuskula-Reimand, L., Hou, H., Samavarchi-Tehrani, P., Rudan, M.V., Liang, M., Medina-Rivera, A., Mohammed, H., Schmidt, D., Schwalie, P., Young, E.J., et al. (2016). Topoisomerase II beta interacts with cohesin and CTCF at topological domain borders. Genome Biol *17*, 182. 10.1186/s13059-016-1043-8.
25. Manville, C.M., Smith, K., Sondka, Z., Rance, H., Cockell, S., Cowell, I.G., Lee, K.C., Morris, N.J., Padget, K., Jackson, G.H., and Austin, C.A. (2015). Genome-wide ChIP-seq analysis of human TOP2B occupancy in MCF7 breast cancer epithelial cells. Biol Open *4*, 1436-1447. 10.1242/bio.014308.
26. Lieberman-Aiden, E., van Berkum, N.L., Williams, L., Imakaev, M., Ragoczy, T., Telling, A., Amit, I., Lajoie, B.R., Sabo, P.J., Dorschner, M.O., et al. (2009). Comprehensive mapping of long-range interactions reveals folding principles of the human genome. Science *326*, 289-293. 10.1126/science.1181369.

27. Tavares-Cadete, F., Norouzi, D., Dekker, B., Liu, Y., and Dekker, J. (2020). Multi-contact 3C reveals that the human genome during interphase is largely not entangled. Nat Struct Mol Biol *27*, 1105-1114. 10.1038/s41594-020-0506-5.
28. Goundaroulis, D., Lieberman Aiden, E., and Stasiak, A. (2020). Chromatin Is Frequently Unknotted at the Megabase Scale. Biophys J *118*, 2268-2279. 10.1016/j.bpj.2019.11.002.
29. Grosberg, A., Rabin, Y., Havlin, S., and Neer, A. (1993). Crumpled Globule Model of the Three-Dimensional Structure of DNA. Europhysics Letters *23*, 373. 10.1209/0295-5075/23/5/012.
30. Grosberg, A.Y., Nechaev, S.K., and Shakhnovich, E.I. (1988). The role of topological constraints in the kinetics of collapse of macromolecules. Journal de Physique *49* (*12*). 10.1051/jphys:0198800490120209500.
31. Polovnikov, K., and Slavov, B. (2023). Topological and nontopological mechanisms of loop formation in chromosomes: Effects on the contact probability. Physical Review E *107*. https://doi.org/10.1103/PhysRevE.107.054135.
32. Polovnikov, K.E., Belan, S., Imakaev, M., Brandao, H., and Mirny, L. (2023). Crumpled polymer with loops recapitulates key features of chromosome organization. Physical Review X (Accepted).
33. Kawamura, R., Pope, L.H., Christensen, M.O., Sun, M., Terekhova, K., Boege, F., Mielke, C., Andersen, A.H., and Marko, J.F. (2010). Mitotic chromosomes are constrained by topoisomerase II-sensitive DNA entanglements. J Cell Biol *188*, 653-663. 10.1083/jcb.200910085.
34. Rosa, A., Di Stefano, M., and Micheletti, C. (2019). Topological Constraints in Eukaryotic Genomes and How They Can Be Exploited to Improve Spatial Models of Chromosomes. Front Mol Biosci *6*, 127. 10.3389/fmolb.2019.00127.
35. Rosa, A., and Everaers, R. (2008). Structure and dynamics of interphase chromosomes. PLoS Comput Biol *4*, e1000153. 10.1371/journal.pcbi.1000153.
36. Sikorav, J.L., and Jannink, G. (1994). Kinetics of chromosome condensation in the presence of topoisomerases: a phantom chain model. Biophys J *66*, 827-837. 10.1016/s0006-3495(94)80859-8.
37. Nielsen, C.F., Zhang, T., Barisic, M., Kalitsis, P., and Hudson, D.F. (2020). Topoisomerase IIalpha is essential for maintenance of mitotic chromosome structure. Proc Natl Acad Sci U S A *117*, 12131-12142. 10.1073/pnas.2001760117.
38. Antonin, W., and Neumann, H. (2016). Chromosome condensation and decondensation during mitosis. Curr Opin Cell Biol *40*, 15-22. 10.1016/j.ceb.2016.01.013.
39. Belaghzal, H., Dekker, J., and Gibcus, J.H. (2017). Hi-C 2.0: An optimized Hi-C procedure for high-resolution genome-wide mapping of chromosome conformation. Methods *123*, 56-65. 10.1016/j.ymeth.2017.04.004.
40. Abramo, K., Valton, A.L., Venev, S.V., Ozadam, H., Fox, A.N., and Dekker, J. (2019). A chromosome folding intermediate at the condensin-to-cohesin transition during telophase. Nat Cell Biol *21*, 1393-1402. 10.1038/s41556-019-0406-2.

41. Naumova, N., Imakaev, M., Fudenberg, G., Zhan, Y., Lajoie, B.R., Mirny, L.A., and Dekker, J. (2013). Organization of the mitotic chromosome. Science *342*, 948-953. 10.1126/science.1236083.
42. Iwai, M., Hara, A., Andoh, T., and Ishida, R. (1997). ICRF-193, a catalytic inhibitor of DNA topoisomerase II, delays the cell cycle progression from metaphase, but not from anaphase to the G1 phase in mammalian cells. FEBS Lett *406*, 267-270. 10.1016/s0014-5793(97)00282-2.
43. Tanabe, K., Ikegami, Y., Ishida, R., and Andoh, T. (1991). Inhibition of topoisomerase II by antitumor agents bis(2,6-dioxopiperazine) derivatives. Cancer Res *51*, 4903-4908.
44. Naughton, C., Avlonitis, N., Corless, S., Prendergast, J.G., Mati, I.K., Eijk, P.P., Cockroft, S.L., Bradley, M., Ylstra, B., and Gilbert, N. (2013). Transcription forms and remodels supercoiling domains unfolding large-scale chromatin structures. Nat Struct Mol Biol *20*, 387-395. 10.1038/nsmb.2509.
45. Zhang, H., Emerson, D.J., Gilgenast, T.G., Titus, K.R., Lan, Y., Huang, P., Zhang, D., Wang, H., Keller, C.A., Giardine, B., et al. (2019). Chromatin structure dynamics during the mitosis-to-G1 phase transition. Nature *576*, 158-162. 10.1038/s41586-019-1778-y.
46. Gibcus, J.H., Samejima, K., Goloborodko, A., Samejima, I., Naumova, N., Nuebler, J., Kanemaki, M.T., Xie, L., Paulson, J.R., Earnshaw, W.C., et al. (2018). A pathway for mitotic chromosome formation. Science *359*. 10.1126/science.aao6135.
47. Rao, S.S., Huntley, M.H., Durand, N.C., Stamenova, E.K., Bochkov, I.D., Robinson, J.T., Sanborn, A.L., Machol, I., Omer, A.D., Lander, E.S., and Aiden, E.L. (2014). A 3D map of the human genome at kilobase resolution reveals principles of chromatin looping. Cell *159*, 1665-1680. 10.1016/j.cell.2014.11.021.
48. Hildebrand, E.M., and Dekker, J. (2020). Mechanisms and Functions of Chromosome Compartmentalization. Trends Biochem Sci *45*, 385-396. 10.1016/j.tibs.2020.01.002.
49. Solovei, I., Kreysing, M., Lanctot, C., Kosem, S., Peichl, L., Cremer, T., Guck, J., and Joffe, B. (2009). Nuclear architecture of rod photoreceptor cells adapts to vision in mammalian evolution. Cell *137*, 356-368. 10.1016/j.cell.2009.01.052.
50. Poleshko, A., Smith, C.L., Nguyen, S.C., Sivaramakrishnan, P., Wong, K.G., Murray, J.I., Lakadamyali, M., Joyce, E.F., Jain, R., and Epstein, J.A. (2019). H3K9me2 orchestrates inheritance of spatial positioning of peripheral heterochromatin through mitosis. Elife *8*. 10.7554/eLife.49278.
51. Falk, M., Feodorova, Y., Naumova, N., Imakaev, M., Lajoie, B.R., Leonhardt, H., Joffe, B., Dekker, J., Fudenberg, G., Solovei, I., and Mirny, L.A. (2019). Heterochromatin drives compartmentalization of inverted and conventional nuclei. Nature *570*, 395-399. 10.1038/s41586-019-1275-3.
52. Smith, C.L., Lan, Y., Jain, R., Epstein, J.A., and Poleshko, A. (2021). Global chromatin relabeling accompanies spatial inversion of chromatin in rod photoreceptors. Sci Adv *7*, eabj3035. 10.1126/sciadv.abj3035.
53. Xu, J., Ma, H., Jin, J., Uttam, S., Fu, R., Huang, Y., and Liu, Y. (2018). Super-Resolution Imaging of Higher-Order Chromatin Structures at Different

Epigenomic States in Single Mammalian Cells. Cell Rep *24*, 873-882. 10.1016/j.celrep.2018.06.085.

54. Haralick, R.M., Shanmugam, K., and Dinstein, I.H. (1973). Textural Features for Image Classification. IEEE Transactions on Systems, Man, and Cybernetics *SMC-3*, 610-621. 10.1109/tsmc.1973.4309314.
55. Bensaude, O. (2011). Inhibiting eukaryotic transcription: Which compound to choose? How to evaluate its activity? Transcription *2*, 103-108. 10.4161/trns.2.3.16172.
56. Polovnikov, K., Nechaev, S., and Tamm, M.V. (2018). Effective Hamiltonian of topologically stabilized polymer states. Soft Matter *14*, 6561-6570. 10.1039/c8sm00785c.
57. Polovnikov, K.E., Nechaev, S., and Tamm, M.V. (2019). Many-body contacts in fractal polymer chains and fractional Brownian trajectories. Phys Rev E *99*, 032501. 10.1103/PhysRevE.99.032501.
58. Halverson, J.D., Lee, W.B., Grest, G.S., Grosberg, A.Y., and Kremer, K. (2011). Molecular dynamics simulation study of nonconcatenated ring polymers in a melt. I. Statics. J Chem Phys *134*, 204904. 10.1063/1.3587137.
59. Halverson, J.D., Smrek, J., Kremer, K., and Grosberg, A.Y. (2014). From a melt of rings to chromosome territories: the role of topological constraints in genome folding. Rep Prog Phys *77*, 022601. 10.1088/0034-4885/77/2/022601.
60. Rosa, A., Becker, N.B., and Everaers, R. (2010). Looping probabilities in model interphase chromosomes. Biophys J *98*, 2410-2419. 10.1016/j.bpj.2010.01.054.
61. Rao, S.S.P., Huang, S.C., Glenn St Hilaire, B., Engreitz, J.M., Perez, E.M., Kieffer-Kwon, K.R., Sanborn, A.L., Johnstone, S.E., Bascom, G.D., Bochkov, I.D., et al. (2017). Cohesin Loss Eliminates All Loop Domains. Cell *171*, 305-320 e324. 10.1016/j.cell.2017.09.026.
62. Hsieh, T.-H.S., Cattoglio, C., Slobodyanyuk, E., Hansen, A.S., Darzacq, X., and Tjian, R. (2021). Enhancer-promoter interactions and transcription are maintained upon acute loss of CTCF, cohesin, WAPL, and YY1. bioRxiv *2021.07.14.452365*. doi: https://doi.org/10.1101/2021.07.14.452365.
63. Mora-Bermudez, F., Gerlich, D., and Ellenberg, J. (2007). Maximal chromosome compaction occurs by axial shortening in anaphase and depends on Aurora kinase. Nat Cell Biol *9*, 822-831. 10.1038/ncb1606.
64. Grosberg, A.Y., and Khokhlov, A.R. (1994). Stastical Physics of Macromolecules (AIP Press).
65. Halverson, J.D., Lee, W.B., Grest, G.S., Grosberg, A.Y., and Kremer, K. (2011). Molecular dynamics simulation study of nonconcatenated ring polymers in a melt. II. Dynamics. J Chem Phys *134*, 204905. 10.1063/1.3587138.
66. Nishimura, K., Fukagawa, T., Takisawa, H., Kakimoto, T., and Kanemaki, M. (2009). An auxin-based degron system for the rapid depletion of proteins in nonplant cells. Nat Methods *6*, 917-922. 10.1038/nmeth.1401.
67. Natsume, T., Kiyomitsu, T., Saga, Y., and Kanemaki, M.T. (2016). Rapid Protein Depletion in Human Cells by Auxin-Inducible Degron Tagging with Short Homology Donors. Cell Rep *15*, 210-218. 10.1016/j.celrep.2016.03.001.
68. Liu, Y., and Dekker, J. (2021). Biochemically distinct cohesin complexes mediate positioned loops between CTCF sites and dynamic loops within chromatin

domains. bioRxiv *2021.08.24.457555*. doi: https://doi.org/10.1101/2021.08.24.457555.

69. Haarhuis, J.H.I., van der Weide, R.H., Blomen, V.A., Yanez-Cuna, J.O., Amendola, M., van Ruiten, M.S., Krijger, P.H.L., Teunissen, H., Medema, R.H., van Steensel, B., et al. (2017). The Cohesin Release Factor WAPL Restricts Chromatin Loop Extension. Cell *169*, 693-707 e614. 10.1016/j.cell.2017.04.013.
70. Schwarzer, W., Abdennur, N., Goloborodko, A., Pekowska, A., Fudenberg, G., Loe-Mie, Y., Fonseca, N.A., Huber, W., Haering, C.H., Mirny, L., and Spitz, F. (2017). Two independent modes of chromatin organization revealed by cohesin removal. Nature *551*, 51-56. 10.1038/nature24281.
71. Shintomi, K., and Hirano, T. (2021). Guiding functions of the C-terminal domain of topoisomerase IIalpha advance mitotic chromosome assembly. Nat Commun *12*, 2917. 10.1038/s41467-021-23205-w.
72. Walther, N., Hossain, M.J., Politi, A.Z., Koch, B., Kueblbeck, M., Odegard-Fougner, O., Lampe, M., and Ellenberg, J. (2018). A quantitative map of human Condensins provides new insights into mitotic chromosome architecture. J Cell Biol *217*, 2309-2328. 10.1083/jcb.201801048.
73. Gerlich, D., Hirota, T., Koch, B., Peters, J.M., and Ellenberg, J. (2006). Condensin I stabilizes chromosomes mechanically through a dynamic interaction in live cells. Curr Biol *16*, 333-344. 10.1016/j.cub.2005.12.040.
74. Bintu, B., Mateo, L.J., Su, J.H., Sinnott-Armstrong, N.A., Parker, M., Kinrot, S., Yamaya, K., Boettiger, A.N., and Zhuang, X. (2018). Super-resolution chromatin tracing reveals domains and cooperative interactions in single cells. Science *362*. 10.1126/science.aau1783.
75. Ran, F.A., Hsu, P.D., Wright, J., Agarwala, V., Scott, D.A., and Zhang, F. (2013). Genome engineering using the CRISPR-Cas9 system. Nat Protoc *8*, 2281-2308. 10.1038/nprot.2013.143.
76. Hsieh, T.S., Fudenberg, G., Goloborodko, A., and Rando, O.J. (2016). Micro-C XL: assaying chromosome conformation from the nucleosome to the entire genome. Nat Methods *13*, 1009-1011. 10.1038/nmeth.4025.
77. Krietenstein, N., Abraham, S., Venev, S.V., Abdennur, N., Gibcus, J., Hsieh, T.S., Parsi, K.M., Yang, L., Maehr, R., Mirny, L.A., et al. (2020). Ultrastructural Details of Mammalian Chromosome Architecture. Mol Cell *78*, 554-565 e557. 10.1016/j.molcel.2020.03.003.
78. Krietenstein, N., and Rando, O.J. (2022). Mammalian Micro-C-XL. Methods Mol Biol *2458*, 321-332. 10.1007/978-1-0716-2140-0_17.
79. Sarkans, U., Gostev, M., Athar, A., Behrangi, E., Melnichuk, O., Ali, A., Minguet, J., Rada, J.C., Snow, C., Tikhonov, A., et al. (2018). The BioStudies database-one stop shop for all data supporting a life sciences study. Nucleic Acids Res *46*, D1266-D1270. 10.1093/nar/gkx965.
80. Eastman, P., and Pande, V.S. (2015). OpenMM: A Hardware Independent Framework for Molecular Simulations. Comput Sci Eng *12*, 34-39. 10.1109/MCSE.2010.27.
81. Arbona, J.M., Herbert, S., Fabre, E., and Zimmer, C. (2017). Inferring the physical properties of yeast chromatin through Bayesian analysis of whole nucleus simulations. Genome Biol *18*, 81. 10.1186/s13059-017-1199-x.

82. Doi, M., and Edwards, S.F. (1988). The Theory of Polymer Dynamics (Oxford University Press).
83. Kremer, K., and Grest, G. (1990). Dynamics of entangled linear polymer melts: A molecular-dynamics simulation. The Journal of Chemical Physics *92*.
84. Nuebler, J., Fudenberg, G., Imakaev, M., Abdennur, N., and Mirny, L.A. (2018). Chromatin organization by an interplay of loop extrusion and compartmental segregation. Proc Natl Acad Sci U S A *115*, E6697-E6706. 10.1073/pnas.1717730115.
85. Davidson, I.F., Bauer, B., Goetz, D., Tang, W., Wutz, G., and Peters, J.M. (2019). DNA loop extrusion by human cohesin. Science *366*, 1338-1345. 10.1126/science.aaz3418.
86. Golfier, S., Quail, T., Kimura, H., and Brugues, J. (2020). Cohesin and condensin extrude DNA loops in a cell cycle-dependent manner. Elife *9*. 10.7554/eLife.53885.
87. Kim, Y., Shi, Z., Zhang, H., Finkelstein, I.J., and Yu, H. (2019). Human cohesin compacts DNA by loop extrusion. Science *366*, 1345-1349. 10.1126/science.aaz4475.
88. Polovnikov, K.E., Gherardi, M., Cosentino-Lagomarsino, M., and Tamm, M.V. (2018). Fractal Folding and Medium Viscoelasticity Contribute Jointly to Chromosome Dynamics. Phys Rev Lett *120*, 088101. 10.1103/PhysRevLett.120.088101.
89. Tamm, M.V., Nazarov, L.I., Gavrilov, A.A., and Chertovich, A.V. (2015). Anomalous diffusion in fractal globules. Physical review letters, *114*, 178102.
90. Ge, T., Panyukov, S., and Rubinstein, M. (2016). Self-similar conformations and dynamics in entangled melts and solutions of nonconcatenated ring polymers. Macromolecules *49*, 708-722.
91. Smrek, J., and Grosberg, A.Y. (2015). Understanding the dynamics of rings in the melt in terms of the annealed tree model. Journal of Physics: Condensed Matter *27*.
92. Walther, N., and Ellenberg, J. (2018). Quantitative live and super-resolution microscopy of mitotic chromosomes. Methods Cell Biol *145*, 65-90. 10.1016/bs.mcb.2018.03.014.
93. Goloborodko, A., Venev, S., Abdennur, N., azkalot1, and Tommaso, P.D. (2019). mirnylab/distiller-nf: v0.3.3 (v0.3.3). Zenodo. https://doi.org/10.5281/zenodo.3350937.
94. Venev, S., Abdennur, N., Goloborodko, A., Flyamer, I., Fudenberg, G., Nuebler, J., Galitsyna, A., Akgol, B., Abraham, S., Kerpedjiev, P., and Imakaev, M. (2022). open2c/cooltools: v0.5.1. Zenodo. 10.5281/zenodo.6324229.
95. Ewels, P., Magnusson, M., Lundin, S., and Kaller, M. (2016). MultiQC: summarize analysis results for multiple tools and samples in a single report. Bioinformatics *32*, 3047-3048. 10.1093/bioinformatics/btw354.
96. Abdennur, N., Goloborodko, A., Imakaev, M., Kerpedjiev, P., Fudenberg, G., Oullette, S., Lee, S., Strobelt, H., Gehlenborg, N., and Mirny, L. (2021). open2c/cooler: v0.8.11 (v0.8.11). Zenodo. https://doi.org/10.5281/zenodo.4655850.

97. Abdennur, N., and Mirny, L.A. (2020). Cooler: scalable storage for Hi-C data and other genomically labeled arrays. Bioinformatics *36*, 311-316. 10.1093/bioinformatics/btz540.
98. Abdennur, N., Goloborodko, A., gfudenberg, Imakaev, M., agalitsyna, Venev, S., Abraham, S., Flyamer, I., Spracklin, G., Chumpitaz, L., and Aafke (2022). open2c/bioframe: v0.3.3. Zenodo. 10.5281/zenodo.6317259.
99. Abdennur, N., Goloborodko, A., gfudenberg, Imakaev, M., Galitsyna, A., Abraham, S., Spracklin, G., Venev, S., Chumpitaz, L., Flyamer, I., and Aafke (2021). open2c/bioframe: v0.3.0 (v0.3.0). Zenodo. https://doi.org/10.5281/zenodo.5348312.
100. Goloborodko, A., Abdennur, N., Venev, S., hbbrandao, and gfudenberg (2019). mirnylab/pairtools v0.3.0 (v0.3.0). Zenodo. https://doi.org/10.5281/zenodo.2649383.
101. Reback, J., jbrockmendel, McKinney, W., Bossche, J.V.d., Augspurger, T., Roeschke, M., Hawkins, S., Cloud, P., gfyoung, Sinhrks, et al. (2022). pandas-dev/pandas: Pandas 1.4.2 (v1.4.2). Zenodo. https://doi.org/10.5281/zenodo.6408044.
102. Harris, C.R., Millman, K.J., van der Walt, S.J., Gommers, R., Virtanen, P., Cournapeau, D., Wieser, E., Taylor, J., Berg, S., Smith, N.J., et al. (2020). Array programming with NumPy. Nature *585*, 357-362. 10.1038/s41586-020-2649-2.
103. team, T.s.d. (2021). scipy/scipy: SciPy 1.7.1 (v1.7.1). Zenodo. https://doi.org/10.5281/zenodo.5152559.
104. Virtanen, P., Gommers, R., Oliphant, T.E., Haberland, M., Reddy, T., Cournapeau, D., Burovski, E., Peterson, P., Weckesser, W., Bright, J., et al. (2020). SciPy 1.0: fundamental algorithms for scientific computing in Python. Nat Methods *17*, 261-272. 10.1038/s41592-019-0686-2.
105. Hunter, J.D. (2007). Matplotlib: A 2D Graphics Environment. Computing in Science & Engineering *9*, 90-95. 10.1109/mcse.2007.55.
106. team, T.m.d. (2021). matplotlib/matplotlib: REL: v3.4.3 (v3.4.3). Zenodo. https://doi.org/10.5281/zenodo.5194481.
107. van der Walt, S., Schönberger, J., Nunez-Iglesias, J., Boulogne, F., Warner, J., Yager, N., Gouillart, E., Yu, T., and contributors., t.s.-i. (2014). scikit-image: image processing in Python. PeerJ *2*. https://doi.org/10.7717/peerj.453.
108. team, T.s.d. (2021). mwaskom/seaborn: v0.11.2 (August 2021) (v0.11.2). Zenodo. https://doi.org/10.5281/zenodo.5205191.
109. Imakaev, M., Fudenberg, G., McCord, R.P., Naumova, N., Goloborodko, A., Lajoie, B.R., Dekker, J., and Mirny, L.A. (2012). Iterative correction of Hi-C data reveals hallmarks of chromosome organization. Nat Methods *9*, 999-1003. 10.1038/nmeth.2148.
110. Venev, S., Abdennur, N., Goloborodko, A., Flyamer, I., Fudenberg, G., Nuebler, J., Galitsyna, A., Akgol, B., Abraham, S., Kerpedjiev, P., and Imakaev, M. (2021). open2c/cooltools: v0.4.0 (v0.4.0). Zenodo. https://doi.org/10.5281/zenodo.4667696.
111. Li, H. (2021). New strategies to improve minimap2 alignment accuracy. Bioinformatics. 10.1093/bioinformatics/btab705.

112. Li, H. (2018). Minimap2: pairwise alignment for nucleotide sequences. Bioinformatics *34*, 3094-3100. 10.1093/bioinformatics/bty191.
113. Stirling, D.R., Swain-Bowden, M.J., Lucas, A.M., Carpenter, A.E., Cimini, B.A., and Goodman, A. (2021). CellProfiler 4: improvements in speed, utility and usability. BMC Bioinformatics *22*, 433. 10.1186/s12859-021-04344-9.

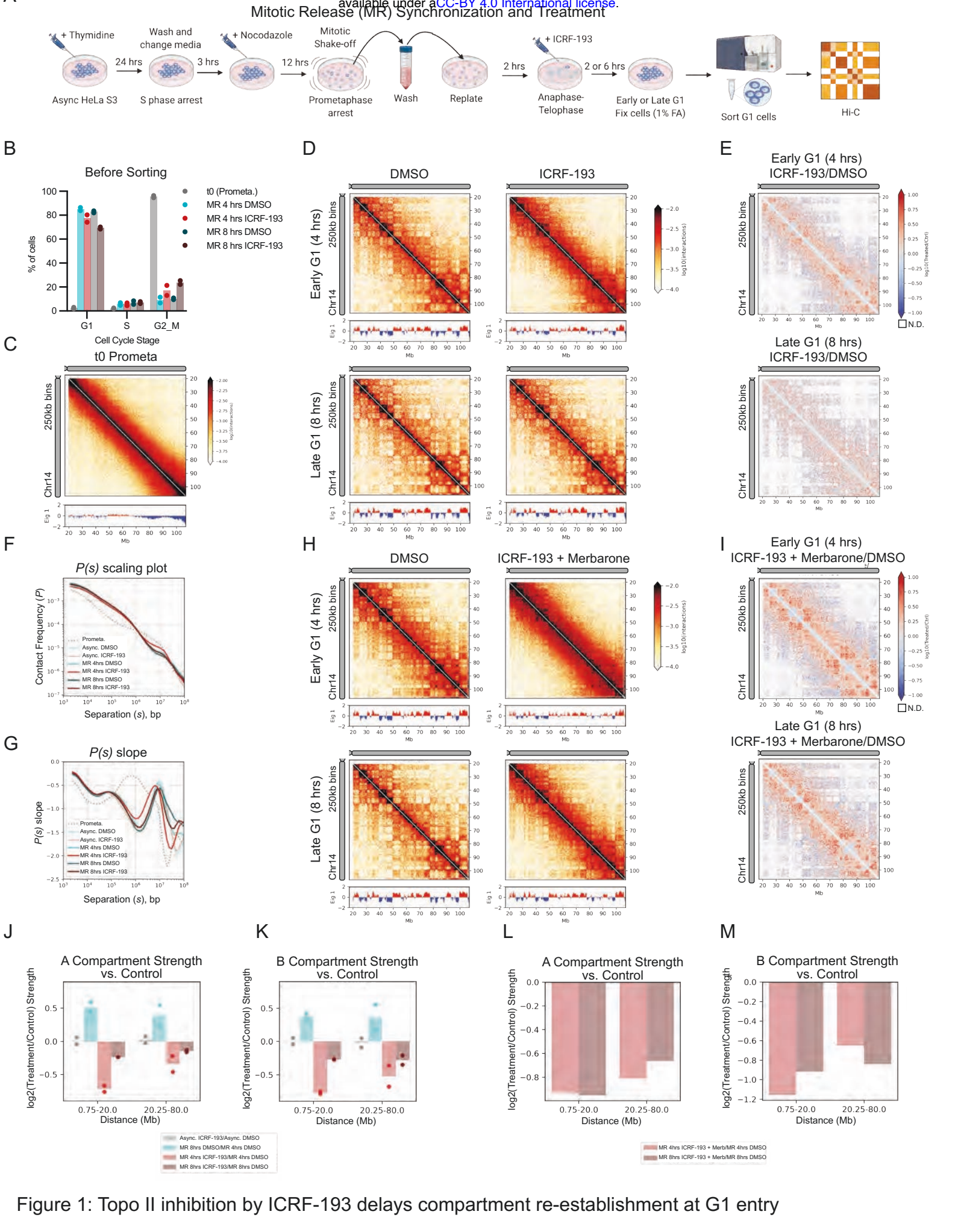

Figure 1: Topo II inhibition by ICRF-193 delays compartment re-establishment at G1 entry

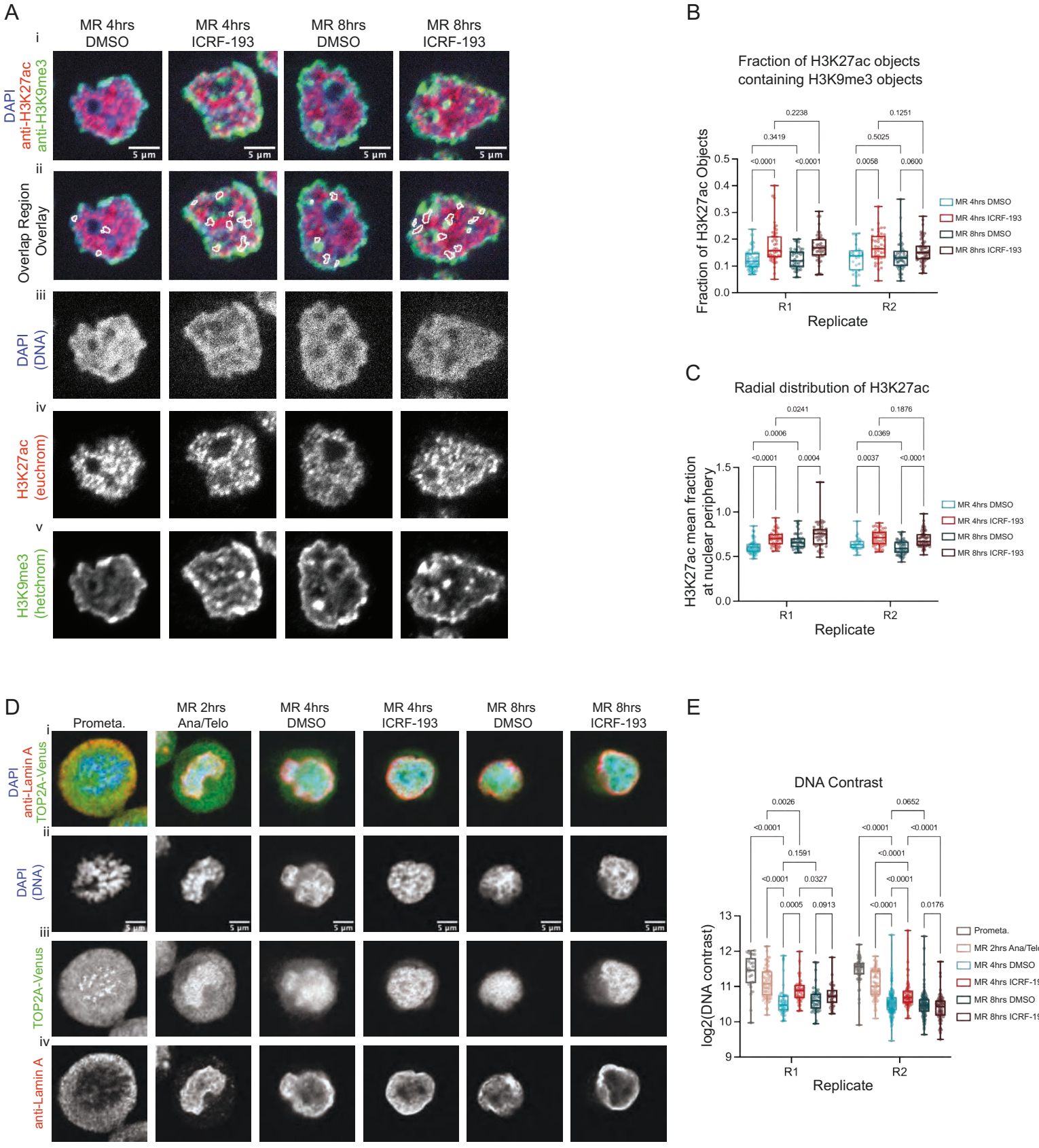

Figure 2: ICRF-193 treatment during G1 entry disrupts nuclear organization and chromosome morphology

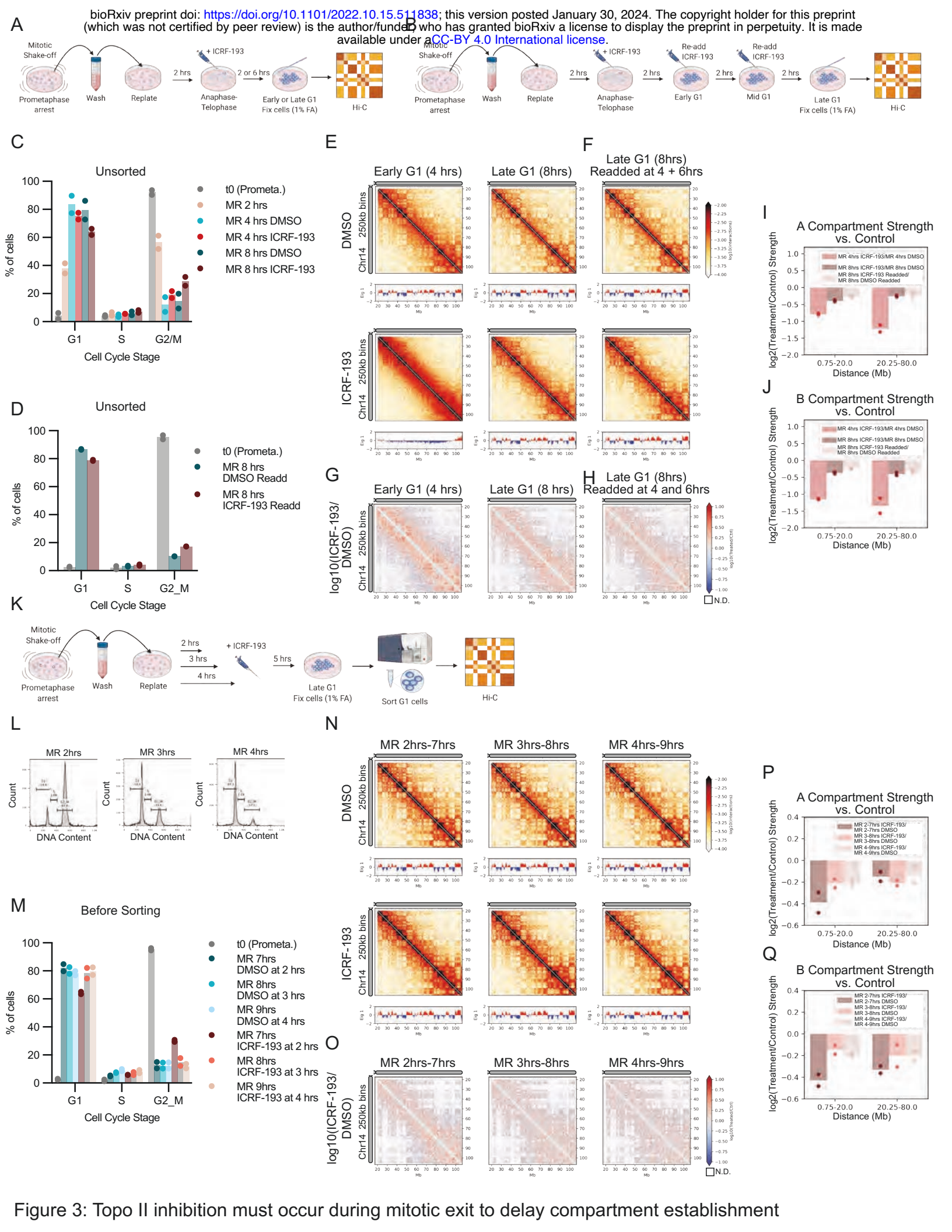

Figure 3: Topo II inhibition must occur during mitotic exit to delay compartment establishment

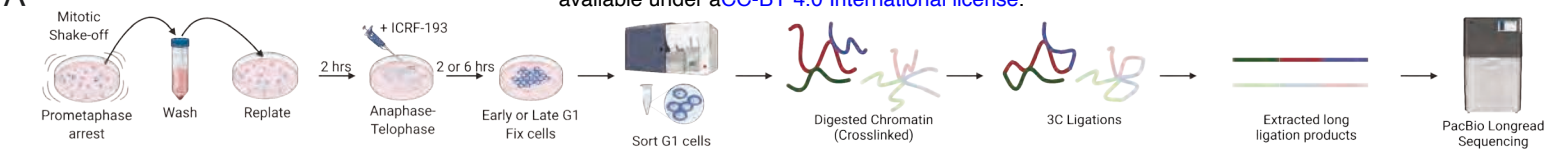

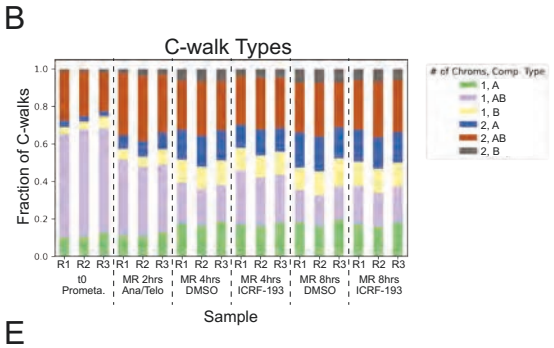

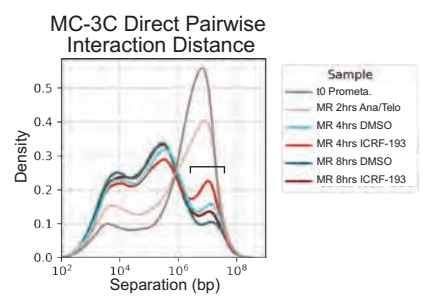

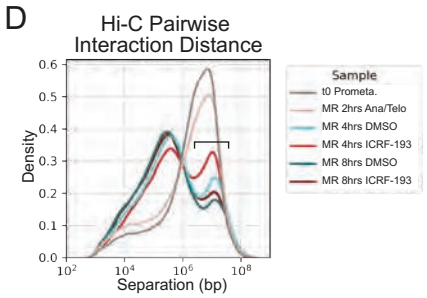

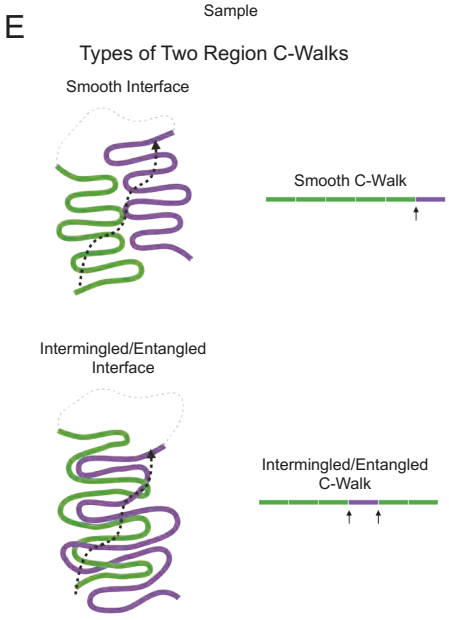

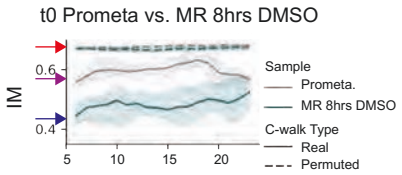

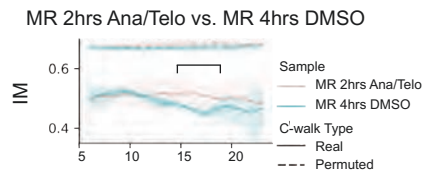

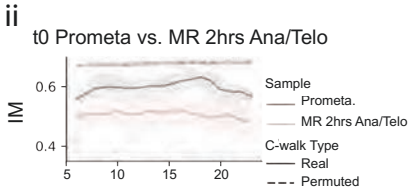

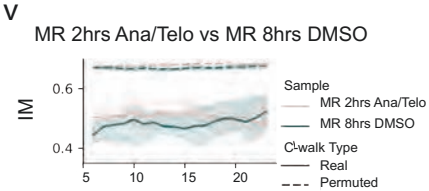

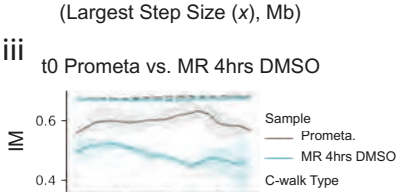

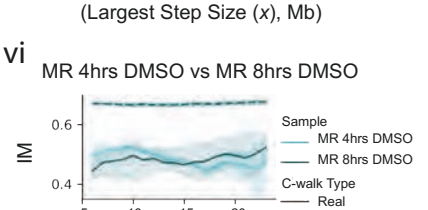

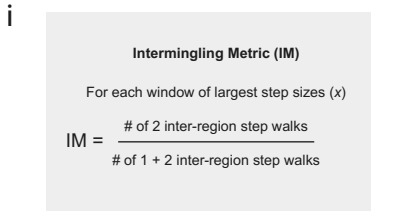

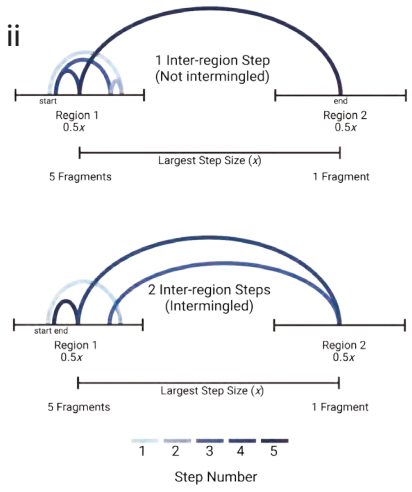

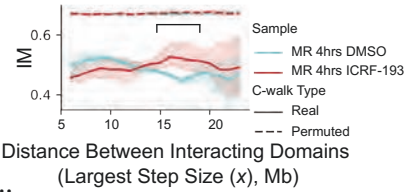

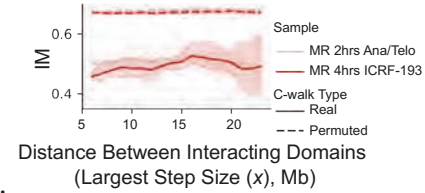

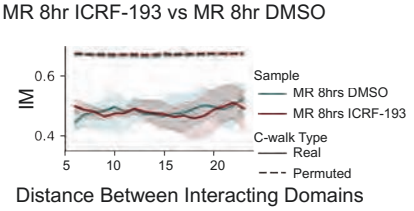

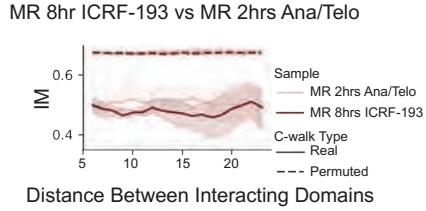

Figure 4: Topo II resolves mitotic entanglements during G1 establishment of interphase chromosome folding

Figure 5: Polymer simulations reveal that hallmarks of mitotic exit with inhibited Topoisomerase II correspond to the entangled mitotic chromosome

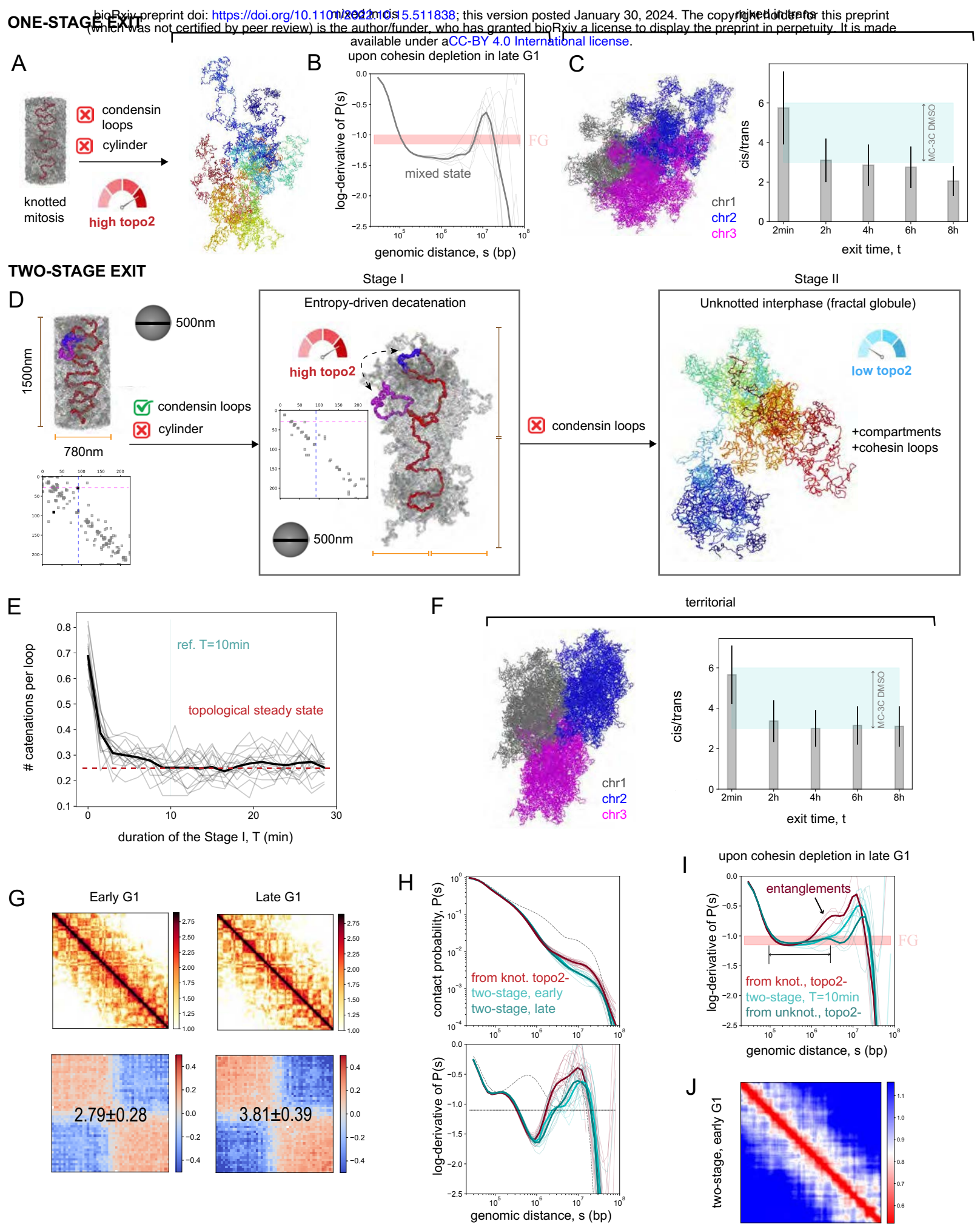

Figure 6. The two-stage model of mitotic exit allows for directed Topo II and removal of most of the mitotic catenations

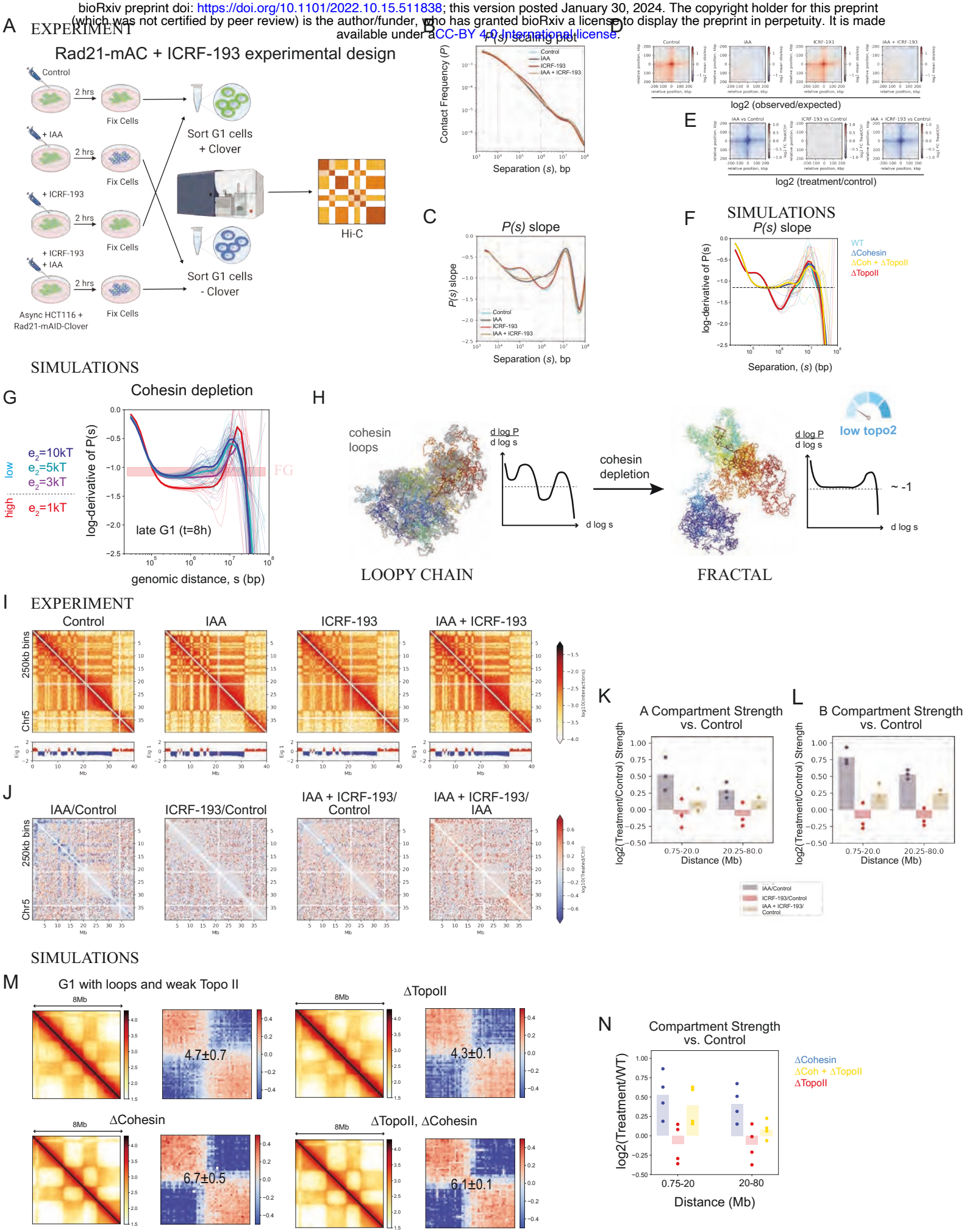

Figure 7: Weak Topo II is required for increased compartment strength upon cohesin depletion